Geophysical Journal International

Advancing Astronomy and Geophysics

doi: 10.1093/gji/ggy495

Geophys. J. Int. (2019) 216, 1364–1393
Advance Access publication 2018 November 22
GJI Geodynamics and tectonics

Spectral-infinite-element simulations of coseismic and post-earthquake deformation

Hom Nath Gharti[®], Leah Langer^{®1} and Jeroen Tromp^{1,2}

¹Department of Geosciences, Princeton University, Princeton, NJ, USA. E-mail: hgharti@princeton.edu

Accepted 2018 November 21. Received 2018 November 7; in original form 2018 May 04

SUMMARY

Accurate and efficient simulations of coseismic and post-earthquake deformation are important for proper inferences of earthquake source parameters and subsurface structure. These simulations are often performed using a truncated half-space model with approximate boundary conditions. The use of such boundary conditions introduces inaccuracies unless a sufficiently large model is used, which greatly increases the computational cost. To solve this problem, we develop a new approach by combining the spectral-element method with the mapped infiniteelement method. In this approach, we still use a truncated model domain, but add a single outer layer of infinite elements. While the spectral elements capture the domain, the infinite elements capture the far-field boundary conditions. The additional computational cost due to the extra layer of infinite elements is insignificant. Numerical integration is performed via Gauss-Legendre-Lobatto and Gauss-Radau quadratures in the spectral and infinite elements, respectively. We implement an equivalent moment-density tensor approach and a split-node approach for the earthquake source, and discuss the advantages of each method. For postearthquake deformation, we implement a general Maxwell rheology using a second-order accurate and unconditionally stable recurrence algorithm. We benchmark our results with the Okada analytical solutions for coseismic deformation, and with the Savage & Prescott analytical solution and the PyLith finite-element code for post-earthquake deformation.

Key words: Moment-density tensor; Split-node; Coseismic deformation; Post-earthquake relaxation; Spectral-infinite-element method.

1 INTRODUCTION

Accurate and efficient simulations of coseismic and post-earthquake deformation are critical for analyses of earthquake slip and subsurface structure (e.g. Kenner & Segall 2000a,b). There are several existing analytical and numerical methods to calculate seismic deformation. Analytical methods are generally limited to simple homogeneous or layered models and are unable to accommodate realistic 3-D material heterogeneity, complex model geometry and topography. Most existing tools based on numerical methods use lower order polynomials to approximate the displacement field. Far-field boundary conditions are generally implemented by considering very large models and imposing Dirichlet boundary conditions. The accuracy and efficiency of these methods can be improved by using geometrically adaptive mesh refinement, specifically *h*-refinement (e.g. Zienkiewicz *et al.* 2005). If the model of interest is already very large, adaptive mesh refinement alone is not efficient.

Okada (1985, 1992) provides the most general analytical solutions for coseismic deformation due to point sources and finite faults in a homogeneous linearly elastic half-space. This method is fast and accurate, and can accommodate complex faults by use of the superposition principle. For a layered half-space, calculations of coseismic and post-earthquake deformation can be performed with analytical and semi-analytical methods (Pollitz 1996, 1992; Barbot & Fialko 2010). Savage & Prescott (1978) built on the work of Nur & Mavko (1974) to develop an analytical method for modelling an earthquake cycle for a semi-infinite fault, including coseismic deformation and post-earthquake relaxation, in a layered half-space consisting of an elastic lithosphere over a Maxwell viscoelastic asthenosphere. The fault is modelled as a screw dislocation. Later, Savage (1998) developed an analytical expression for an edge dislocation in a layered half-space. The normal-mode approach (Piersanti *et al.* 1995) and spectral finite-element method (FEM, Tanaka *et al.* 2009) have been used to compute post-earthquake relaxation for spherically symmetric earth models. The FEM is probably the most widely used numerical method to model seismic deformation. Williams & Richardson (1991) used the FEM to produce a layered viscoelastic model of the San Andreas fault. Reilinger *et al.* (2000) developed an FEM model with viscous and elastic zones. More recent studies based on the FEM accommodate more complex

²Program in Applied & Computational Mathematics, Princeton University, Princeton, NJ, USA

material models and realistic Earth structure (Masterlark 2003; Hu *et al.* 2004; Zhao *et al.* 2004; Freed *et al.* 2006; Parker *et al.* 2008; Kyriakopoulos *et al.* 2013; Agata *et al.* 2018; Wang & Fialko 2018). The most commonly used FEM package is PyLith (Aagaard *et al.* 2013a), which can simulate 3-D coseismic and post-earthquake deformation in a variety of settings. A detailed analysis of PyLith and comparisons with our method may be found in Section 4.2.3.

Earthquake sources are characterized by slip vectors that represent displacement discontinuities on a fault. Due to the inherent geometrical discontinuity, numerical implementation of the earthquake source is not trivial. Numerical methods to implement the earthquake source can broadly be classified as the moment-density tensor approach and the split-node approach. In the moment-density tensor approach, an equivalent moment-density tensor is computed from prescribed slip on an earthquake fault. This moment-density tensor is implemented as a force—or load—in the model domain. Since this approach does not explicitly describe slip on the mesh, the mesh does not have to honor the fault surface (Frankel & Vidale 1992; Komatitsch & Tromp 1999; Komatitsch & Vilotte 1998).

In the split-node approach, the mesh is created so that it honors the fault surface, and appropriate slip is explicitly prescribed on both sides of the fault. Because the slip discontinuity has to be enforced, the nodes on the fault surface must split apart. The force contributed by the slip is computed via the stiffness matrix, which can be done locally. Another way to prescribe slip is to consider the slip condition as a constraint on the governing equation based on a penalty approach, Lagrange multiplier, or perturbed Lagrangian method (Zienkiewicz & Taylor 2005). Such methods introduce additional unknown variables at the fault nodes, which generally requires a special technique for the matrix solution. Aagaard *et al.* (2001) implemented the fault by defining six translational degrees of freedom for a node located on the fault surface, such that each side of a fault node has three degrees of freedom, moving relative to each other. The open-source package PyLith uses the Lagrange multiplier method (Aagaard *et al.*2013a).

For numerical simulations of seismic deformation, the half-space is generally truncated and Dirichlet boundary conditions are imposed. These boundary conditions are designed to approximate real-world conditions, but are not fully accurate and can introduce artifacts at the edges of the model domain. The most common approach to this problem uses very large model volumes in an attempt to suppress boundary artifacts. In this approach, local or adaptive mesh refinement is introduced so that a coarser mesh is used near the outer boundary. This strategy requires large computational resources and generally results in only limited improvement (Tsynkov 1998). Alternatively, Robin boundary conditions can be used to mimic far-field boundary conditions (Pollitz 2014).

A better solution to this problem is to make use of infinite-element boundary conditions. In solid and fluid mechanics, the displacement descent approach (Bettess 1977; Medina & Taylor 1983; El-Esnawy *et al.* 1995) and the coordinates ascent approach (Beer & Meek 1981; Zienkiewicz *et al.* 1983; Kumar 1985; Angelov 1991) are both widely used to solve vanishing infinite boundary conditions. In the displacement descent approach, an element in the physical domain is mapped to an element in a natural domain of interval $[0, \infty]$. This is achieved by multiplying the standard interpolation functions by suitable decay functions. Since the integration interval is $[0, \infty]$, classical Gauss–Legendre quadrature cannot be employed. Either Gauss–Legendre quadrature has to be modified to accommodate the $[0, \infty]$ interval, or Gauss–Laguerre quadrature can be used (Mavriplis 1989). The Jacobian of the mapping and the numerical quadrature must be modified from the classical FEM.

The coordinate ascent approach is also referred to as the 'mapped infinite-element' method. In this approach, an element that extends to infinity in the physical domain is mapped to a standard natural element with interval [-1, 1]. This is achieved by defining shape functions using a reference point which serves as the pole of the decaying functions of choice. The corresponding shape functions possess singularities at infinity. Unlike in the displacement descent approach, only the Jacobian of the mapping must be modified, and quadrature identical to the classical FEM method can be used. Kenner & Segall (1999) previously used infinite elements to mimic the far-field boundary conditions to simulate seismic deformation.

To simulate coseismic and post-earthquake deformation, we combine the infinite-element approach based on coordinate ascent with the spectral-element method (SEM). The SEM is a higher-order FEM which uses nodal quadrature, specifically, Gauss—Legendre—Lobatto (GLL) quadrature. Due to the coincidence of the interpolation and quadrature points, pre- and post-processing are efficient and accurate. The method is widely used for dynamic problems, for example seismic and acoustic wave propagation (Faccioli *et al.* 1997; Peter *et al.* 2011; Seriani & Oliveira 2008; Tromp *et al.* 2008) and fluid dynamics (Patera 1984; Canuto *et al.* 1988; Deville *et al.* 2002), and more recently for quasistatic problems (Gharti *et al.* 2012a,b). For post-earthquake deformation problems, 1-D and 2.5-D spectral-element methods are used, respectively, for spherically symmetric earth models (Crawford *et al.* 2017) and axisymmetric models (Pollitz 2014).

We refer to the combination of the spectral-element method with the infinite-element method as the spectral-infinite-element method (SIEM). The SIEM has been used to calculate background gravity (Gharti & Tromp 2017) and gravity anomalies (Gharti et al. 2018) for complex 3-D models. This paper details the development and implementation of the SIEM for seismic deformation. We model coseismic and post-earthquake deformation for a variety of faults to illustrate and validate our method.

2 FORMULATION

2.1 Governing equation

We solve the quasi-static equation that governs coseismic and post-earthquake deformation in a setting illustrated in Fig. 1. The domain of interest, Ω , is embedded in a quasi-half-space. The embedded domain has a boundary consisting of a free surface Γ_0 and an artificial

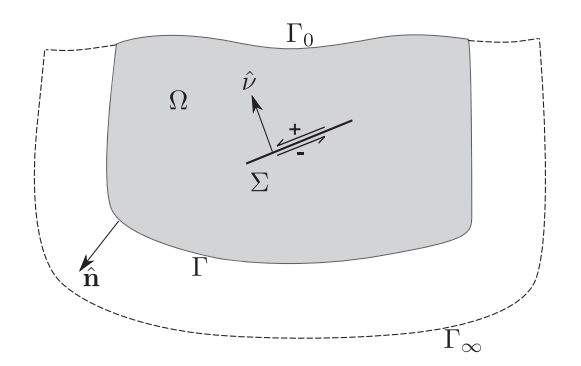


Figure 1. Schematic diagram of a fault buried in a quasi-half-space.

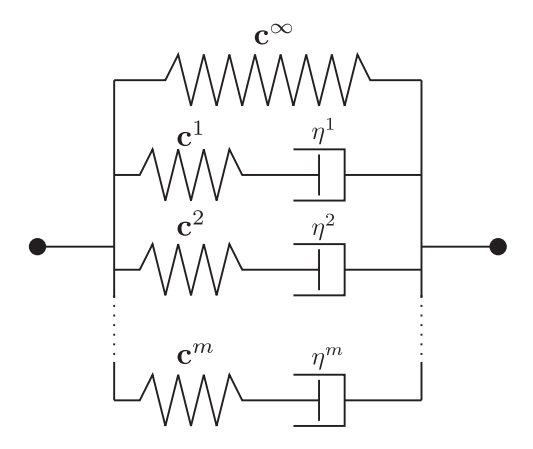


Figure 2. Schematic diagram of the generalized Maxwell rheology.

boundary Γ . The half-space has a boundary consisting of Γ_0 and a remainder Γ_∞ . The unit outward normal to the domain boundary is denoted by $\hat{\bf n}$. The domain Ω contains a fault surface Σ with unit normal $\hat{\bf v}$.

The governing equation in the domain of interest, Ω , is given by

$$\nabla \cdot \mathbf{T} + \mathbf{f} = \mathbf{0},\tag{1}$$

subject to the boundary condition

$$\hat{\mathbf{n}} \cdot \mathbf{T} = \mathbf{0} \tag{2}$$

on the free surface Γ_0 . Here **T** denotes the stress tensor, and **f** denotes an external body force. Coseismic deformation is controlled by the elastic constitutive relation $\mathbf{T} = \mathbf{c} : \boldsymbol{\varepsilon}$, where **c** denotes the fourth-order elastic tensor and $\boldsymbol{\varepsilon}$ the strain tensor. Post-earthquake deformation is controlled by a generalized Maxwell rheology, which is described in the next section.

2.2 Viscoelastic rheology

We use a generalized Maxwell rheology to simulate the viscoelastic response. A generalized Maxwell model, shown in Fig. 2, consists of a single elastic element (a spring) in parallel with a number of Maxwell elements (a spring and a dashpot in series). For simplicity, we assume an isotropic model with a viscoelastic response restricted to the deviatoric stress only.

The constitutive equation for a generalized Maxwell solid is given by (Zienkiewicz & Taylor 2005)

$$\mathbf{T}(t) = \mathbf{c}^{\infty} : \boldsymbol{\varepsilon}(t) + \sum_{m=1}^{M} \mathbf{c}^{m} : \mathbf{q}^{m}(t), \tag{3}$$

where ε denotes the strain tensor, η^m the viscosity of the *m*th dashpot, and *M* the total number of Maxwell elements. The elastic modulus of the elastic element is denoted by \mathbf{c}^{∞} , and \mathbf{c}^m denotes the elastic modulus of the *m*th Maxwell element, so that the total modulus \mathbf{c} is determined by

$$\mathbf{c} = \mathbf{c}^{\infty} + \sum_{m=1}^{M} \mathbf{c}^{m}. \tag{4}$$

The Maxwell rheology is a special case, for which $\mathbf{c}^{\infty} = \mathbf{0}$ and m = 1.

For linear viscoelasticity, the partial strain $\mathbf{q}^m(t)$ is the solution to the first-order differential equation

$$\dot{\mathbf{q}}^m + \mathbf{q}^m / \tau^m = \dot{\boldsymbol{\varepsilon}},\tag{5}$$

where $\tau^m = \eta^m/E^m$ is the relaxation time and E^m Young's modulus of the mth Maxwell element.

For an isotropic model, we can split the stress into two components:

$$\mathbf{T} = \mathbf{\tau} - p \mathbf{I} \quad , \qquad p = -\frac{1}{3} \operatorname{tr}(\mathbf{T}), \tag{6}$$

where τ denotes the stress deviator, I the identity tensor, and p the mean stress. Similarly, the strain can be decomposed as

$$\boldsymbol{\varepsilon} = \mathbf{d} + \frac{1}{3} \operatorname{tr}(\boldsymbol{\varepsilon}) \mathbf{I},\tag{7}$$

where **d** is the strain deviator and tr(e) the relative volume change. The mean pressure can be expressed as:

$$p = -\kappa \operatorname{tr}(\boldsymbol{\varepsilon}), \tag{8}$$

where κ denotes the elastic bulk modulus. Now we can express the deviatoric stress in terms of the partial strains as

$$\tau(t) = 2 \mu \left[r^{\infty} \varepsilon(t) + \sum_{m=1}^{M} r^{m} \mathbf{q}^{m}(t) \right], \tag{9}$$

where μ is the shear modulus. Here we have defined moduli ratios for the elastic element, $r^{\infty} = \mu^{\infty}/\mu$, and for the Maxwell elements, $r^{m} = \mu^{m}/\mu$, such that $r^{\infty} + \sum_{m=1}^{M} r^{m} = 1$, in accordance with eq. (4).

For the time-stepping procedure, we may use a recurrence relationship for partial strains (Simo & Hughes 1998; Zienkiewicz & Taylor 2005). For the variables in the following equations, a subscript represents the time step and a superscript represents a Maxwell element. The partial strain at time $t_{n+1} = t_n + \Delta t$ may be computed as

$$\mathbf{q}_{n+1}^{m} = \exp(-\Delta t/\tau^{m}) \, \mathbf{q}_{n}^{m} + \Delta \mathbf{q}_{n+1}^{m}, \tag{10}$$

where Δt is the time step, and where we initialize $\mathbf{q}_0^m = \mathbf{d}_0$. For discrete time steps, we may approximate the partial strain rate in each time step as

$$\Delta \mathbf{q}_{n+1}^{\mathbf{m}} = \Delta q_{n+1}^{\mathbf{m}} (\mathbf{d}_{n+1} - \mathbf{d}_n) \quad , \tag{11}$$

where

$$\Delta q_{n+1}^m = \frac{1}{\Delta t} \left[1 - \exp(-\Delta t / \tau^m) \right]. \tag{12}$$

This approximation is singular for $\Delta t = 0$ and is therefore unstable for very small time steps, but it has a limit value of 1 at $\Delta t = 0$. Thus, we can use a series expansion for smaller values of Δt , namely

$$\Delta q_{n+1}^{m} = 1 - \sum_{\alpha=2}^{\infty} (-1)^{\alpha} \frac{1}{\alpha!} \left(\frac{\Delta t}{\tau^{m}}\right)^{\alpha-1}$$

$$= 1 - \frac{1}{2} \left(\frac{\Delta t}{\tau^{m}}\right) + \frac{1}{3!} \left(\frac{\Delta t}{\tau^{m}}\right)^{2} - \frac{1}{4!} \left(\frac{\Delta t}{\tau^{m}}\right)^{3} + \cdots$$
(13)

This series quickly converges, and in practice we need only a few, say less than five, terms to achieve convergence. In our examples, we set a stopping tolerance of 10^{-12} .

Using the recursion formula, the constitutive eq. (9) becomes

$$\tau_{n+1}(t) = 2\mu \left[r^{\infty} \mathbf{d}_{n+1}(t) + \sum_{m=1}^{M} r^{m} \mathbf{q}_{n+1}^{m}(t) \right]. \tag{14}$$

Finally, the tangent shear modulus is given by

$$\frac{\partial \boldsymbol{\tau}_{n+1}}{\partial \boldsymbol{\varepsilon}_{n+1}} = 2 \,\mu \left(r^{\infty} + \sum_{m=1}^{M} r^{m} \Delta q_{n+1}^{m} \right) \left(\mathsf{E} - \frac{1}{3} \mathbf{I} \otimes \mathbf{I} \right),\tag{15}$$

where E denotes the fourth-order identity tensor with elements $E_{ijk\ell} = \frac{1}{2}(\delta_{ik}\delta_{j\ell} + \delta_{i\ell}\delta_{jk})$. For small time steps $\Delta t \to 0$, the tangent shear modulus is equal to the full shear modulus, whereas for very large time steps $\Delta t \to \infty$, it is equal to the equilibrium shear modulus $\mu^{\infty} = r^{\infty}\mu$. This viscoelastic time stepping procedure is second-order accurate and unconditionally stable.

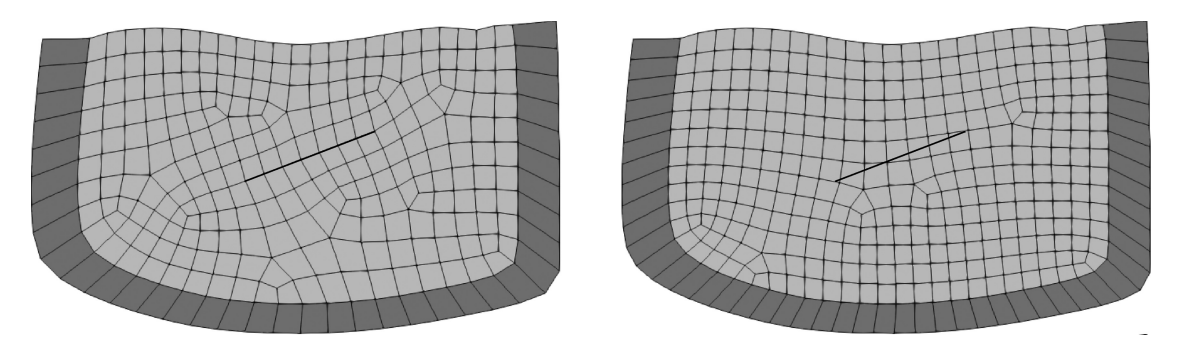


Figure 3. The domain of interest, Ω , is discretized using spectral elements (light grey elements). A single layer of infinite elements is added outside the domain (dark grey elements). Black thick line represents the fault. Left-hand panel: mesh honors the fault. Right-hand panel: mesh does not honor the fault.

2.3 Earthquake source

An earthquake source is defined in terms of slip vector Δs on a fault plane Σ . The slip vector captures a discontinuity in the displacement field s when going from the + side of the fault Σ to the - side (see Fig. 1) (Dahlen & Tromp 1998; Aki & Richards 2002):

$$\Delta \mathbf{s} = \mathbf{s}^{+} - \mathbf{s}^{-} = [\mathbf{s}]_{-}^{+}. \tag{16}$$

The notation $[\cdot]_{-}^{+}$ captures a jump in the enclosed quantity when going from the + to the - side of the fault. For a sliding fault, the normal component of displacement must be continuous across the fault, i.e., $\hat{\mathbf{v}} \cdot \Delta \mathbf{s} = 0$. One can also introduce a discontinuous traction on the fault, $\Delta \mathbf{t} = [\hat{\mathbf{v}} \cdot \mathbf{T}]_{-}^{+}$. However, for a spontaneous rupture, there is no externally applied forces, and consequently, the traction must be continuous: $\Delta \mathbf{t} = \mathbf{0}$ (Aki & Richards 2002).

An earthquake source is usually implemented using one of two general methods: the split-node approach and the moment-density tensor approach, as we discuss in the following two sections.

2.3.1 Split-node approach

For the split-node approach, we need to mesh the model domain Ω so that the element boundaries honor the fault surface, as shown in Fig. 3(a). We use a strategy first suggested by Melosh & Raefsky (1981), in which slip is equally divided on the + and - sides of the fault. In this strategy, the node on the + side has displacement $\tilde{s} + \Delta s/2$ and the node on the - side has displacement $\tilde{s} - \Delta s/2$, where \tilde{s} is an unknown mean displacement that must be solved for. Only Δs is known and contributes to the force. The force induced by the prescribed slip may be computed using the stiffness matrix, as discussed in Section 2.5. The prescribed slip only induces an external force and does not constrain the fault nodes. Therefore, the split-node approach does not alter the number of the degrees of freedom in the system. In the split-node approach, the body force f in the governing eq. (1) is zero because the load is introduced by prescribing a discontinuous displacement field on the fault surface.

We have implemented slip tapering in our package using two approaches. When using the split-node approach, users can turn on the built-in tapering option, which sets zero slip on the fault boundary and accommodates the linear slip variation along the tapering direction within all elements on the fault edge. Both the split-node and moment-density tensor approaches allow the user to specify a general taper by defining variable slip on the fault.

2.3.2 Moment-density tensor approach

Given the slip vector Δs and the unit fault normal \hat{v} the moment density tensor **m** is determined by (Dahlen & Tromp 1998; Aki & Richards 2002):

$$\mathbf{m} = \mathbf{c} : \hat{\mathbf{v}} \Delta \mathbf{s},\tag{17}$$

where **c** denotes the fourth-order elastic tensor. Because of the symmetries of the elastic tensor, the moment-density tensor is symmetric: $\mathbf{m} = \mathbf{m}^T$, where T denotes the transpose. We note that eq. (17) is a general expression representing both shear and tensile faults.

Since slip is confined to the fault surface Σ , an equivalent external body force may be used in the governing eq. (1) to represent the source using a Dirac delta function (Dahlen & Tromp 1998):

$$\mathbf{f}(\mathbf{x}) = -\mathbf{m}(\mathbf{x}_{\Sigma}) \cdot \nabla \delta(\mathbf{x} - \mathbf{x}_{\Sigma}). \tag{18}$$

Here \mathbf{x}_{Σ} denotes locations on the fault surface where slip is defined. Since the slip does not have to be explicitly defined on the fault nodes, the mesh does not have to honor the fault surface, as shown in Fig. 3(b).

2.4 Weak form

The weak form of the governing eq. (1) may be obtained by taking the dot product with an arbitrary test vector \mathbf{w} and integrating over the domain of interest Ω :

$$\int_{\Omega} \mathbf{w} \cdot (\nabla \cdot \mathbf{T}) \, \mathrm{d}V + \int_{\Omega} \mathbf{w} \cdot \mathbf{f} \, \mathrm{d}V = 0. \tag{19}$$

Upon substituting the source representation (18) for the moment-density tensor approach and using Gauss' theorem, we obtain

$$\int_{\Omega} \nabla \mathbf{w} : \mathbf{T} \, \mathrm{d}V = \int_{\Gamma} \mathbf{w} \cdot \mathbf{T} \cdot \mathbf{n} \, \mathrm{d}S + \mathbf{m}(\mathbf{x}_{\Sigma}) : \nabla \mathbf{w}(\mathbf{x}_{\Sigma}), \tag{20}$$

where we have used the traction-free boundary condition (2). Note that the moment-density tensor source only contributes to the integral for points located on the fault plane.

2.5 Discretization

To solve the problem using a spectral-element method (SEM), the domain Ω is meshed using spectral elements. A single layer of infinite elements is added outside the domain to reproduce an infinite domain, as shown in Fig. 3. As we discuss in more detail in Section 2.7, spectral and infinite elements share the same interpolation functions, namely Lagrange polynomials, but use different quadratures. Thus, the displacement field \mathbf{s} is discretized in natural coordinates $\boldsymbol{\xi}$ as

$$\mathbf{s}(\boldsymbol{\xi}) = \sum_{\alpha=1}^{n} \mathbf{s}_{\alpha} N_{\alpha}(\boldsymbol{\xi}), \tag{21}$$

where \mathbf{s}_{α} denotes the displacement at quadrature point $\boldsymbol{\xi}_{\alpha}$ and N_{α} is an interpolation function. The total number of quadrature points in an element is denoted by n, and is given by the product of the number of quadrature points in each dimension, n^{j} , j = 1, 2, 3; that is, $n = \prod_{j=1}^{3} n^{j}$. The interpolation functions N_{α} in natural coordinates are determined by the tensor product of one-dimensional Lagrange polynomials, that is

$$N_{\alpha^{j}}^{j}(\xi^{j}) = \prod_{\beta=1 \atop \beta \neq \alpha^{j}}^{n^{j}} \frac{(\xi^{j} - \xi_{\beta}^{j})}{(\xi_{\alpha^{j}}^{j} - \xi_{\beta}^{j})},$$
(22)

such that

$$N_{\alpha}(\xi) = \prod_{j=1}^{3} N_{\alpha^{j}}^{j}(\xi^{j}). \tag{23}$$

Here α denotes the index of quadrature point $\boldsymbol{\xi}_{\alpha} = \{\xi_{\alpha^1}, \xi_{\alpha^2}, \xi_{\alpha^3}\}.$

A component of the test function \mathbf{w} is taken to be an interpolation function N_{α} , making the approach a Galerkin method. Upon substituting such a test function and the displacement field given by eq. (21) in eq. (20), we obtain a set of elemental linear equations that may be written conveniently in matrix–vector form:

$$\mathsf{K}_{e}\,\mathsf{S}_{e}=\mathsf{F}_{e}.\tag{24}$$

The quantities K_e and F_e are known, respectively, as the stiffness matrix and force vector of an element. The elemental displacement vector, S_e , has the form

$$S_{e} = \begin{bmatrix} s_{1}^{x} & s_{1}^{y} & s_{1}^{z} & s_{2}^{x} & s_{2}^{y} & s_{2}^{z} & s_{3}^{x} & s_{3}^{y} & s_{3}^{z} & \cdots & s_{n}^{x} & s_{n}^{y} & s_{n}^{z} \end{bmatrix}^{\mathsf{T}}, \tag{25}$$

with 3n entries for the three components of displacement at each of the n quadrature points. The transpose of a vector or matrix is denoted by T. Symbolically, we may write the elemental stiffness matrix, K_e , as

$$\mathbf{K}_{e} = \int_{\Omega_{e}} \mathbf{B}_{e}^{\mathsf{T}} \mathbf{C} \, \mathbf{B}_{e} \, \mathrm{d}V, \tag{26}$$

where Ω_e denotes element e and C denotes the 3D elasticity tensor stored as a 6 × 6 matrix, and B_e is the strain-displacement matrix given by

$$B_e = S N_n^T. (27)$$

Here we have defined the matrix operator

$$S = \begin{bmatrix} \frac{\partial}{\partial x} & 0 & 0\\ 0 & \frac{\partial}{\partial y} & 0\\ 0 & 0 & \frac{\partial}{\partial z} \\ \frac{\partial}{\partial y} & \frac{\partial}{\partial x} & 0\\ 0 & \frac{\partial}{\partial z} & \frac{\partial}{\partial y} \\ \frac{\partial}{\partial z} & 0 & \frac{\partial}{\partial x} \end{bmatrix}, \tag{28}$$

and the interpolation function matrix

$$\mathbf{N}_{e} = \begin{bmatrix}
N_{1} & 0 & 0 & N_{2} & 0 & 0 & N_{3} & 0 & 0 & \cdots & N_{n} & 0 & 0 \\
0 & N_{1} & 0 & 0 & N_{2} & 0 & 0 & N_{3} & 0 & \cdots & 0 & N_{n} & 0 \\
0 & 0 & N_{1} & 0 & 0 & N_{2} & 0 & 0 & N_{3} & \cdots & 0 & 0 & N_{n}
\end{bmatrix}^{\mathsf{T}}.$$
(29)

For the split-node approach, the force vector takes the form

$$F_{e} = -\frac{1}{2} \left(K_{e}^{+} - K_{e}^{-} \right) \Delta S_{e} + \int_{\Gamma} N_{e} t \, dS, \tag{30}$$

where ΔS_e is the elemental slip vector, which has nonzero values only on fault surface nodes. Similarly, the matrices K_e^+ and K_e^- are evaluated on the + and - sides of the fault surface, respectively. The traction vector t is defined by

$$\mathbf{t} = \begin{bmatrix} t^x & t^y & t^z \end{bmatrix}^\mathsf{T}.\tag{31}$$

Alternatively, for the moment-density tensor approach, the force vector takes the form

$$\mathsf{F}_e = \mathsf{G}^\mathsf{T} \mathsf{M} + \int_{\Gamma} \mathsf{N}_e \, \mathsf{t} \, \mathsf{d}S,\tag{32}$$

where

$$G = \begin{bmatrix} \frac{\partial N_e}{\partial x} & \frac{\partial N_e}{\partial y} & \frac{\partial N_e}{\partial z} \end{bmatrix}^{\mathsf{T}},\tag{33}$$

$$\mathsf{M} = \begin{bmatrix} m_{11} & m_{12} & m_{13} & m_{21} & m_{22} & m_{23} & m_{31} & m_{32} & m_{33} \end{bmatrix}^\mathsf{T}. \tag{34}$$

After assembling the elemental matrices and vectors, we obtain a set of global linear equations

$$KS = F \quad , \tag{35}$$

where K and F are known, respectively, as the global stiffness matrix and the global force vector. Similarly, S is the global displacement vector.

2.6 Artificial boundary

The simulation domain Ω is terminated by an artificial boundary Γ , as Fig. 1 shows. This boundary gives rise to an unknown contribution to the force vectors (32) and (30), namely $\int_{\Gamma} N_e \, t \, dS$. One option is to simply assume that this boundary is sufficiently far from the fault surface Σ that this contribution can be safely ignored, because the traction vanishes asymptotically. Another option is to force the displacement vector to be zero on the artificial boundary, under the assumption that the displacement field decays sufficiently fast. In common practice, the normal component of displacement on the boundary is set to zero.

A better approach is to add a so-called infinite-element layer to the domain Ω along its artificial boundary Γ , as Fig. 3 illustrates. The outer surface of this infinite-element layer captures the imaginary boundary at infinity, that is Γ_{∞} in Fig. 1. In this approach, we split the global force vector, F, in terms of an unknown part, $F_1 = \int_{\Gamma_{\infty}} N_e \, t \, dS$ and a known part, \hat{F}_2 . Similarly, the global displacement vector S is split in terms of a known component, \hat{S}_1 , corresponding to displacement values on Γ_{∞} which are zero, and an unknown component, S_2 , which corresponds to the rest of the domain. Therefore, we may partition the global equation as follows:

$$\begin{bmatrix} \mathbf{K}_{11} & \mathbf{K}_{12} \\ \mathbf{K}_{21} & \mathbf{K}_{22} \end{bmatrix} \begin{bmatrix} \hat{\mathbf{S}}_1 \\ \mathbf{S}_2 \end{bmatrix} = \begin{bmatrix} \mathbf{F}_1 \\ \hat{\mathbf{F}}_2 \end{bmatrix}. \tag{36}$$

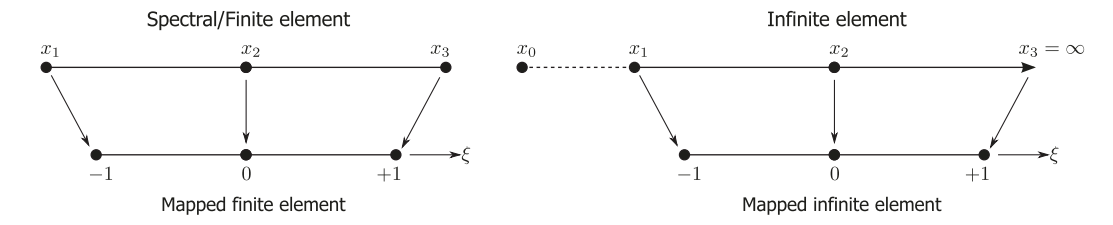


Figure 4. Mapping of a 1-D element to natural coordinates. The element consists of three geometrical nodes. Left-hand panel: spectral/finite element. Right-hand panel: infinite element.

This results in two sets of linear equations:

$$K_{12} S_2 = F_1 \tag{37}$$

and

$$K_{22}S_2 = \hat{F}_2$$
 , (38)

where we have used the fact that $\hat{S}_1 = 0$. First, the unknown part S_2 is obtained by solving eq. (38). Once S_2 is determined, F_1 can be directly obtained from eq. (37), if necessary. In practice, we form the global matrix corresponding to only the unknown degrees of freedom, that is K_{22} , so a matrix partition is never required.

2.7 Mapping

For numerical integration, a point $\mathbf{x} = \{x^i\}$ in a physical element is mapped to a point $\boldsymbol{\xi} = \{\xi^j\}$ in the natural element. This mapping is different for the spectral-element and infinite-element domains, as we describe.

2.7.1 Spectral elements

A spectral element is mapped to the natural element using the transformation

$$\mathbf{x}(\boldsymbol{\xi}) = \sum_{\alpha} \mathbf{x}_{\alpha} M_{\alpha}(\boldsymbol{\xi}). \tag{39}$$

Here M_{α} denotes a shape function and n_g is the number of geometrical nodes, \mathbf{x}_{α} , of an element. The shape function M_{α} is defined similarly to the interpolation function (eq. 21). However, the number of interpolation points n and the number of geometrical points n_g may differ. In general, $n_g < n$ for the spectral-element method, leading to a sub-parametric formulation. The Jacobian matrix of the transformation is determined using the relation $J^{ij}(\xi) = \partial x^i(\xi)/\partial \xi^j$. For integration, we use GLL quadrature, in which the interpolation and quadrature points are identical.

2.7.2 Infinite elements

Inside the domain Ω , geometrical nodes are used to map an element from the physical domain to the natural domain (Fig. 4a). Outside the domain Ω , we introduce a single layer of elements in which the displacement field is discretized using infinite elements (Fig. 3). For simplicity and clarity, we illustrate a 1-D mapping. A point known as the pole, x_0 , and an intermediate geometrical node, x_2 , are used to map the element from the physical domain to the natural domain (Fig. 4b) using the transformation (Curnier 1983; Zienkiewicz *et al.* 1983)

$$x = M_0(\xi) x_0 + M_2(\xi) x_2, \tag{40}$$

where the shape functions $M_0(\xi)$ and $M_2(\xi)$ are defined as

$$M_0(\xi) = \frac{-\xi}{1 - \xi},$$

$$M_2(\xi) = 1 + \frac{\xi}{1 - \xi}.$$
(41)

The shape functions $M_0(\xi)$ and $M_2(\xi)$ satisfy the relation

$$M_0(\xi) + M_2(\xi) = 1. (42)$$

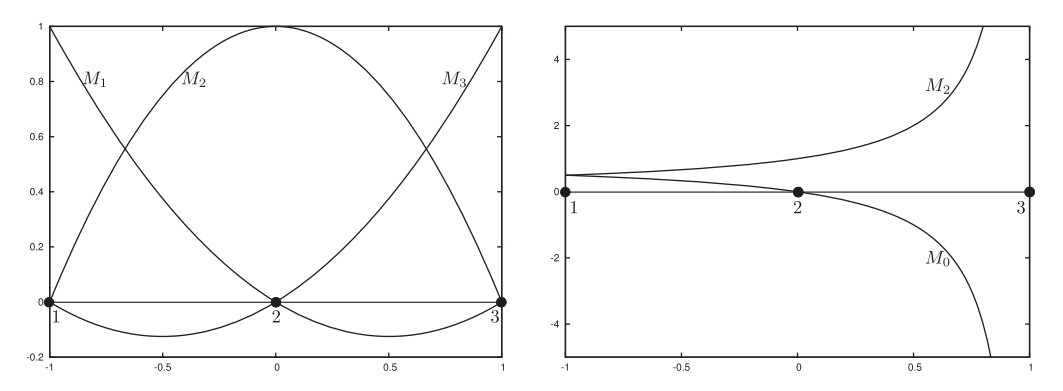


Figure 5. Shape functions for a 1-D element with three geometrical nodes. Left-hand panel: spectral/finite element. Right-hand panel: infinite element.

These shape functions map an element in the physical domain, which is extended to infinity, to an element in the natural domain in the following manner (Fig. 4b):

$$\xi = -1$$
 $x = x_1,$
 $\xi = 0$ $x = x_2,$
 $\xi = +1$ $x = x_3 = \infty.$ (43)

For infinite elements, shape functions therefore become singular at $\xi = 1$. Shape functions for regular spectral and infinite elements are plotted in Fig. 5.

To understand the consequence of infinite-element shape functions, we can express the displacement field, s, as a piecewise polynomial

$$\mathbf{s}(\xi) = \mathbf{a}_0 + \mathbf{a}_1 \, \xi + \mathbf{a}_2 \, \xi^2 + \mathbf{a}_3 \, \xi^3 + \cdots \,. \tag{44}$$

From eqs (40) and (41) we determine the inverse map

$$\xi = 1 - \frac{\gamma (x_1 - x_0)}{r},\tag{45}$$

where $\gamma = (x_2 - x_0)/(x_1 - x_0)$ is a constant, given x_0 , x_1 , and x_2 , and $r = x - x_0$. The value of γ governs the location of the pole, x_0 , and hence the size of the infinite element.

Substituting ξ in eq. (44), we obtain

$$\mathbf{s}(r) = \mathbf{b}_0 + \frac{\mathbf{b}_1}{r} + \frac{\mathbf{b}_2}{r^2} + \frac{\mathbf{b}_3}{r^3} + \cdots, \tag{46}$$

where \mathbf{b}_0 , \mathbf{b}_1 , \mathbf{b}_2 , are constant vectors for given x_0 , x_1 , and x_2 . Hence, the value of $\mathbf{s}(r)$ decays to \mathbf{b}_0 when r tends to ∞ . For our problem, since the displacement decays to zero at ∞ , the value of \mathbf{b}_0 is zero. One or more poles may be necessary depending on the physics and the model. All poles have to be located opposite to the decay direction and outside the infinite element. For the coseismic and post-earthquake deformation problems, we generally set the source location as the pole. The accuracy of the infinite-element approximation may be increased by increasing the order of the interpolation functions, but the shape functions remain the same. Alternative shape functions for infinite elements have been suggested (Marques & Owen 1984; Kumar 1985). Shape functions can be generalized to particular decay functions, such as exponential or logarithmic decay (Abdel-Fattah *et al.* 2000). A typical mapping of a 3-D infinite element in a general physical domain to an element in the natural domain is shown in Fig. 6.

2.8 Numerical integration

In a spectral element, we use GLL quadrature:

$$\int_{-1}^{1} f(\xi) \, \mathrm{d}\xi = w_1 \, f(-1) + \sum_{n=2}^{n-1} w_\alpha \, f(\xi_\alpha) + w_n \, f(1), \tag{47}$$

where f is a general function, w_{α} are the GLL weights of integration, and ξ_{α} are the quadrature points. GLL quadrature is exact for polynomials of order 2n-3 or less.

Infinite elements, however, cannot use GLL quadrature due to the singularity at infinity. To circumvent this problem, we choose to use Gauss-Radau quadrature, which is given by

$$\int_{-1}^{1} f(\xi) \, \mathrm{d}\xi = w_1 \, f(-1) + \sum_{\alpha=2}^{n} w_\alpha \, f(\xi_\alpha). \tag{48}$$

Gauss-Radau quadrature is exact for polynomials of order 2n-2 or less, and includes only the near end points of the interval. Since the quadrature does not include the end points of the interval, infinite-element shape functions can be computed at all quadrature points.

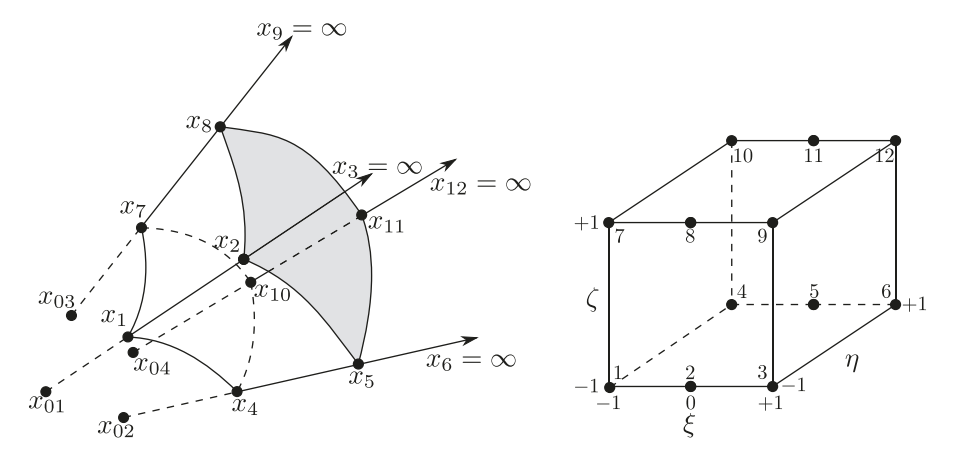


Figure 6. Left-hand panel: a general 3-D infinite element. Points x_{01} , x_{02} , x_{03} and x_{04} are the poles. Right-hand panel: 3-D infinite element mapped to its natural coordinates.

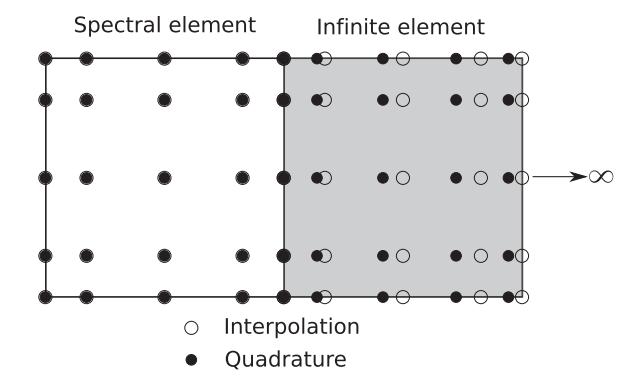


Figure 7. Coupling between a spectral element and an infinite element in 2-D. Both elements use identical interpolation nodes. Spectral elements use Gauss—Lobatto—Legendre (GLL) quadrature points, while infinite elements use Gauss—Radau (GR) quadrature points in the infinite direction and GLL quadrature in the two remaining directions. GLL and GR quadrature points coincide on a spectral-infinite element boundary.

By combining Gauss-Radau quadrature in infinite elements with GLL quadrature in spectral elements, quadrature points on an spectral-infinite element interface coincide (Fig. 7). This coincidence naturally couples spectral and infinite elements. Alternatively, one can use Gauss-Lengendre quadrature.

2.9 Computing model differences

In Section 4, we benchmark our code against analytical solutions from Okada (1992) and FEM solutions from PyLith (Aagaard *et al.* 2013a). The error between our solution and the reference solution is calculated by integrating over the differences at the GLL points, using the formulation described in Section 2.8. This integrated difference is normalized by the integrated reference displacement, so that our error estimate becomes

$$\operatorname{Error}^{2} = \frac{\int_{\Omega} ||\hat{\mathbf{s}} - \mathbf{s}||^{2} \, \mathrm{d}V}{\int_{\Omega} ||\hat{\mathbf{s}}||^{2} \, \mathrm{d}V}.$$
(49)

Here \hat{s} and s are reference and numerical solutions, respectively. Source elements are not included in the integration. Differences for each component of displacement are calculated by integrating over that component of the displacement instead of the full displacement vector.

3 PARALLELIZATION

For parallelization, we use non-overlapping domain decomposition, in which each partition contains a unique set of elements and nodes are only shared on interfaces. Since infinite elements and spectral elements have similar pre- and post-processing procedures, infinite elements do not pose any difficulty for parallelization. We use Message Passing Interface (MPI) as a parallel library (Gropp *et al.* 1994) and the SCOTCH mesh partitioning package for mesh decomposition (Pellegrini & Roman 1996). We implemented parallel iterative Krylov solvers using PETSc, a portable and extensible toolkit for scientific computation (Balay *et al.* 2015).

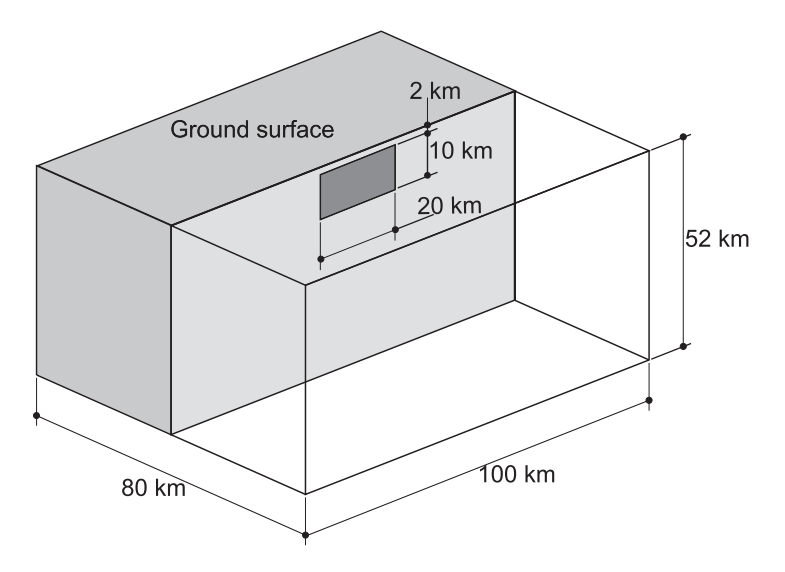


Figure 8. Model geometry of the vertical fault. The model is cut through the centre so that the fault is visible. The fault surface is shown in dark grey.

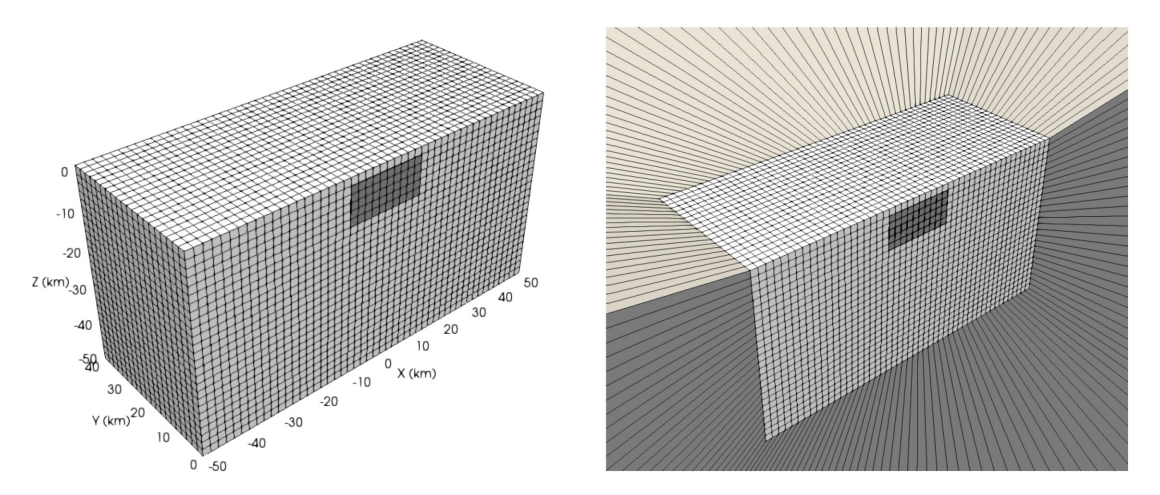


Figure 9. Left-hand panel: spectral-element mesh of a vertical fault model. The model is cut to reveal the fault. Right-hand panel: infinite elements (outer grey) radiating from the outer surfaces of the model. The fault surface is shown in dark gray. The SEM uses the mesh in the left and the SIEM uses the mesh in the right.

4 EXAMPLES

We rely on MeshAssist (Gharti *et al.* 2017) and Trelis/CUBIT (CUBIT 2017) for model preparation and meshing for all examples included in this article. All simulations use 3 GLL points in each direction, resulting in a total of 27 points per element. For reasons of accuracy and consistency, we solve all examples in a nondimensionalized framework. We use a conjugate gradient solver with block Jacobi preconditioning, and we set a relative tolerance of 10^{-6} as a stopping criterion for the solver.

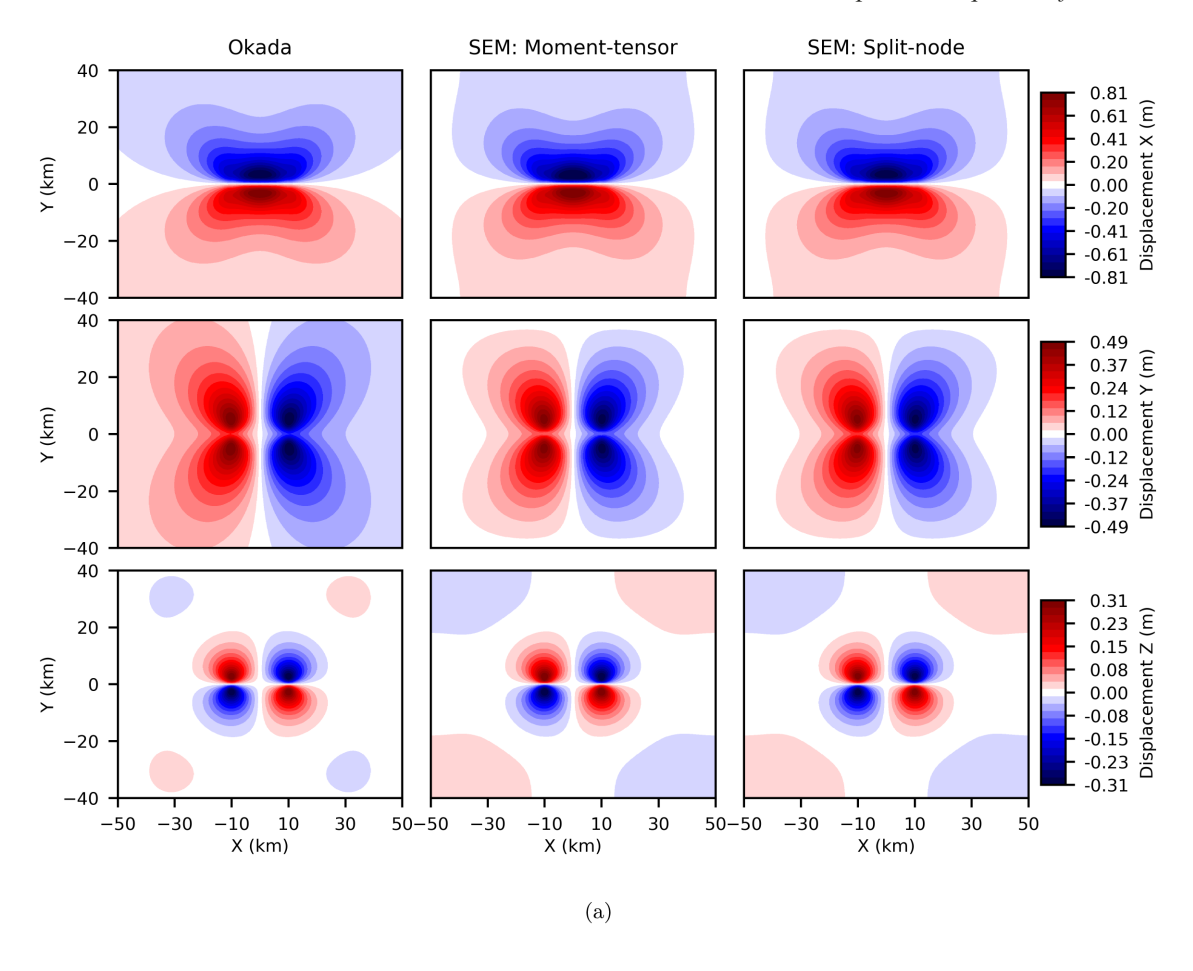
4.1 Elastic benchmarks

In the following examples, we compute coseismic deformation and compare with the Okada solutions. We adapted the Okada analytical solution routine 'DC3D' (Okada 1992) to calculate the reference solutions. We note that the Okada analytical expressions depend only on a single elasticity parameter, namely Poisson's ratio.

4.1.1 Vertical strike-slip fault

We consider a homogeneous model of size $100 \text{ km} \times 80 \text{ km} \times 52 \text{ km}$ with a vertical fault of size $20 \text{ km} \times 10 \text{ km}$, as shown in Fig. 8. The center of the fault is located at 7 km depth. We use homogeneous material properties with a Young's modulus of $5.68 \times 10^{10} \text{ N m}^{-2}$ and a Poisson's ratio of 0.25.

The model is meshed using hexahedral elements with an average size of 2 km, resulting in a total number of 52 000 spectral elements, 433 593 points, and 1 300 779 degrees of freedom. The mesh honors the fault surface, as Fig. 9(a) shows. This is essential for the split-node



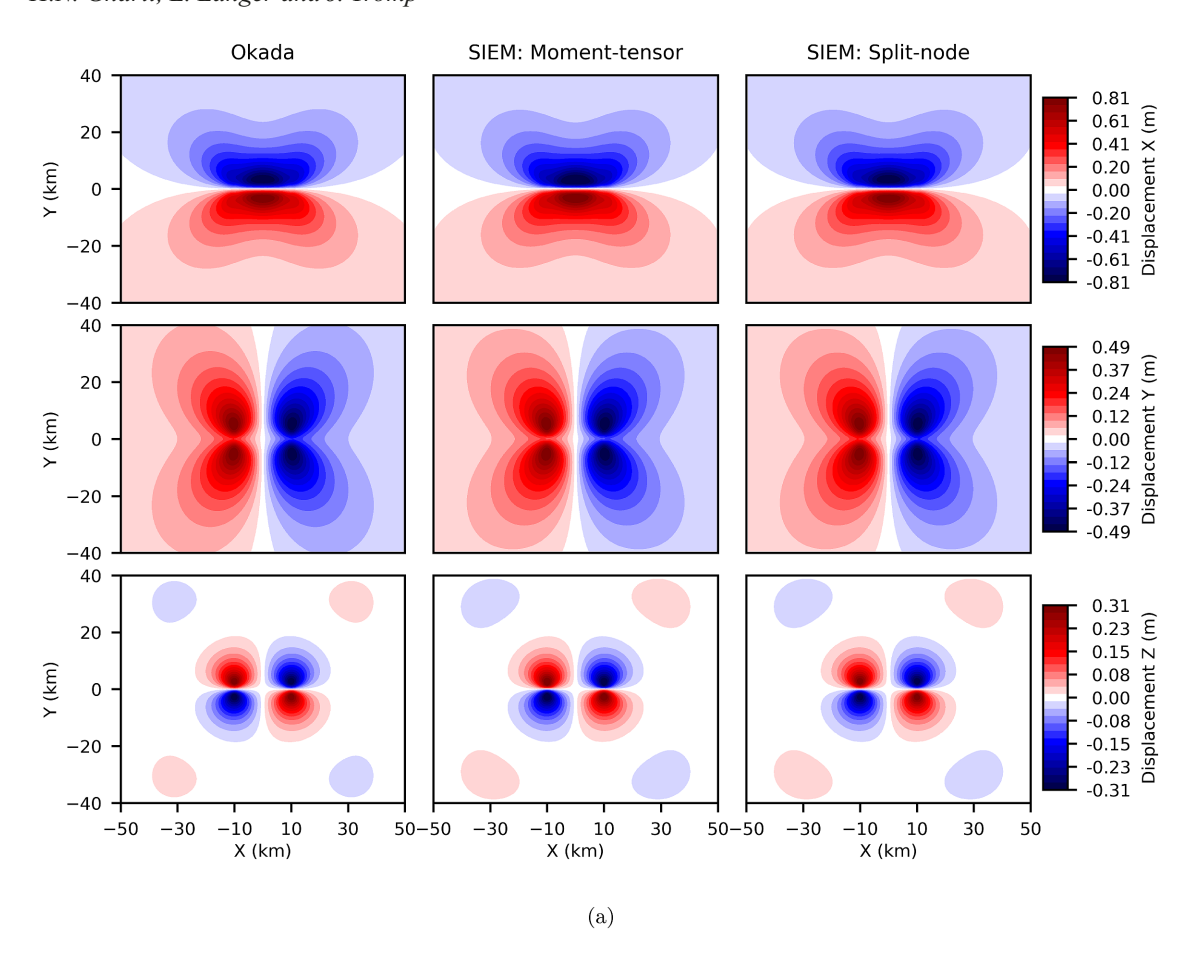
	Differences between SEM and Okada results			
(b)	Component	CMT solution	Split-node solution	
	X component	.125	.123	
	Y component	.476	.478	
	Z component	.215	.215	
	Total	.266	.265	

Figure 10. (a) Displacement field computed with the spectral-element method (SEM) on the free surface for the vertical strike-slip fault. Rows top to bottom: *x*-, *y*- and *z*-components. Columns left to right: Okada analytical solution, SEM with moment-density tensor approach, and SEM with split-node approach. (b) Differences between the SEM and Okada results calculated with eq. (49).

approach but not for the moment-density tensor approach. However, a mesh designed for the split-node approach can also be used for the moment-density tensor approach.

First, a vertical strike-slip source is defined by slip of 5 m along strike. A traction-free boundary condition is imposed on the top surface and Dirichlet boundary conditions are imposed on all lateral and bottom surfaces, so that the normal component of the displacement vanishes, that is $\hat{\mathbf{n}} \cdot \mathbf{s} = 0$. We perform simulations with both the moment-density tensor and the split-node approaches.

In Fig. 10, we plot the displacement field on the free surface and compare it with the Okada solution. The numerical results are in good agreement with the Okada solution, but we observe clear discrepancies on all components. The main lobes around the source are nicely reproduced. Discrepancies due to the truncated boundary are visible near the boundaries, which is expected because the boundaries are not far from the fault. The results for the moment-density tensor and split-node approaches look very similar. For closer inspection, we plot a profile for each displacement component along the y-axis at x = -10 km, shown in Fig. 12 in the left-hand column. We observe that the numerical results are generally in good agreement with the Okada solution for the x- and z-components of the displacement. For the y-component, the discrepancies are significant. Close to the fault, the split-node approach gives better results than the moment density-tensor approach. This is



	Differences between SIEM and Okada results			
(b)	Component	CMT SIEM	Split-node SIEM	
	X component	.019	.008	
	Y component	.020	.018	
	Z component	.021	.018	
	Total	.020	.013	

Figure 11. (a) Displacement field computed with the spectral-infinite-element method (SIEM) on the free surface for the vertical strike-slip fault. Rows top to bottom: *x*-, *y*-, and *z*-components. Columns left to right: Okada analytical solution, SIEM with moment-density tensor approach, and SIEM with split-node approach. (b) Differences between the SIEM and Okada results calculated with eq. (49).

expected because the slip is exactly satisfied on the fault surface in the split-node approach. Near the boundary, both numerical results are similar and are significantly different from the Okada solution.

The significant differences, in particular for the *y*-component, indicate that the model domain we used is not sufficiently large to minimize boundary effects. For the next experiment, we use the same small model domain but add a single layer of infinite elements, as shown in Fig. 9(b). Specifically, a total of 6680 infinite elements are created for this model, which is \approx 13 per cent of the original number of elements. The percentage of infinite elements generally decreases for large models. The infinite-element layer facilitates the implementation of a Dirichlet boundary condition at infinity, that is $\mathbf{s} = \mathbf{0}$ at ∞ . Note that the mesh in the infinite element layer satisfies the non-converging condition at infinity, since opposite faces diverge. We take the center of the source as the pole position for the infinite element mapping. We use the SIEM to simulate coseismic deformation with both the moment-density tensor and split-node approaches. The resulting displacement fields are plotted in Fig. 11. In this case, both numerical results are in excellent agreement with the Okada solution. All displacement components near the boundary are nicely reproduced by both the moment-density tensor and split-node approaches. Just by adding a single layer of elements, we are able to improve the results significantly.

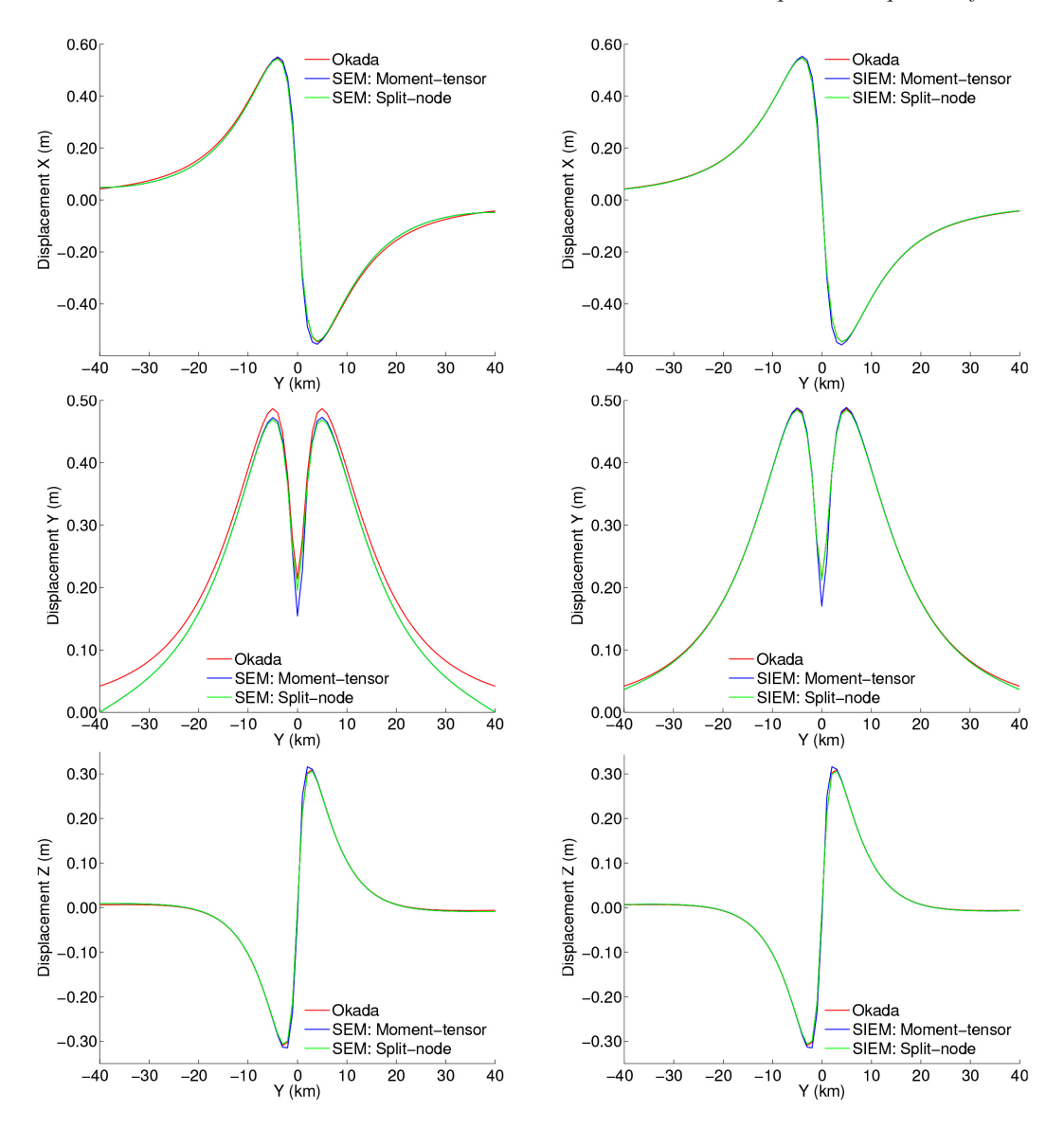


Figure 12. Profiles of the displacement field plotted along y-axis at x = -10 km on the top surface for the vertical strike-slip fault. Top to bottom rows are x-, y-, and z-components, respectively. Left-hand column: SEM. Right-hand column: SIEM.

For a clearer picture, we plot profiles for each displacement component along the y-axis at $x = -10\,$ km, as shown in the right column of Fig. 12. We observe excellent agreement between the Okada and the numerical solutions. Near the fault, the split-node approach gives better results than the moment-density tensor approach due to the exact slip defined on the fault nodes. For the y-component the results are markedly improved. It is interesting to note that the infinite elements improve the result not only near the boundary, but also near the fault.

Finally, we perform a convergence test for this example. We perform simulations with both moment-density tensor and split-node approaches for three different element sizes: 4, 2 and 1 km.

Figs 13 and 14 show snapshots of the displacement fields computed for the different element sizes on the free surface for moment-density tensor and slip-node approaches, respectively. We have interpolated all results on a structured grid of identical resolution for these snapshots. We observe excellent convergence for both approaches. For the moment-density tensor approach, we observe a slight discrepancy around the fault centre for the coarsest mesh with respect to the other two mesh sizes. For the split-node approach snapshots, discrepancies between the coarse and fine mesh results are unnoticeable.

4.1.2 Vertical tensile fault

For this example, we consider a tensile source with a fault opening of 5 m. We use the same model domain, properties, and mesh as in the previous example.

First we impose a traction-free boundary condition on the top surface and Dirichlet boundary conditions for the normal component of displacement on all lateral and bottom surfaces. We run simulations with both the moment-density tensor and the split-node approaches.

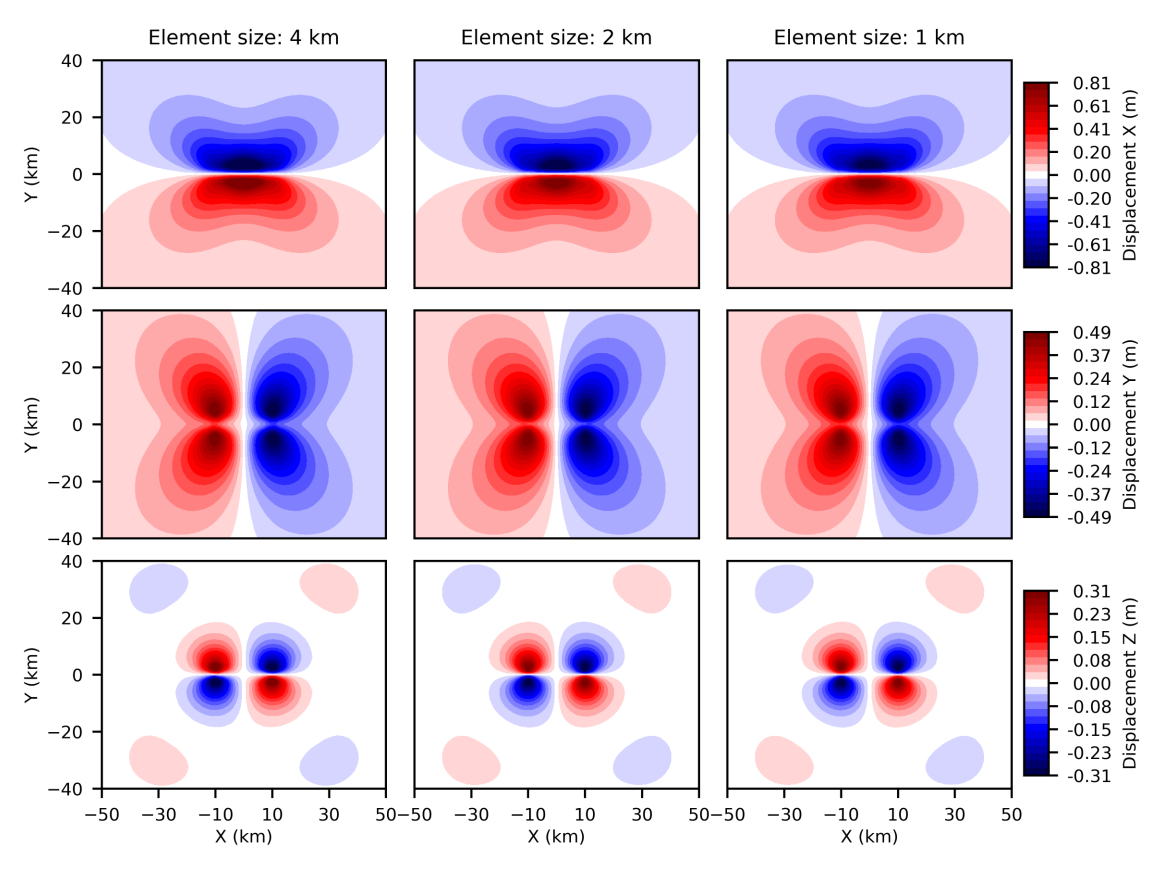


Figure 13. Displacement field computed with the SIEM on the free surface for the vertical strike-slip fault for different mesh refinements with the moment-density tensor approach. Rows top to bottom: *x*-, *y*-, and *z*-components. Columns left to right: element sizes 4, 2 and 1 km.

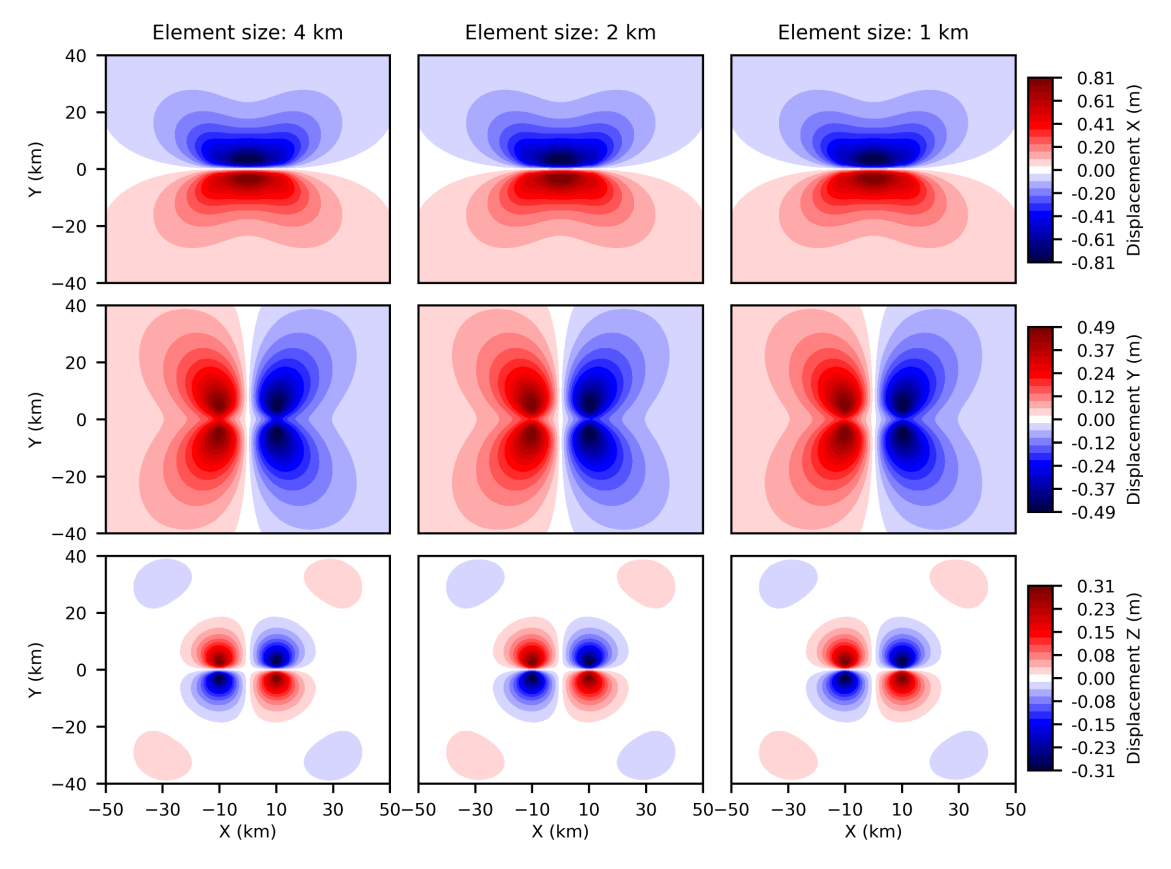
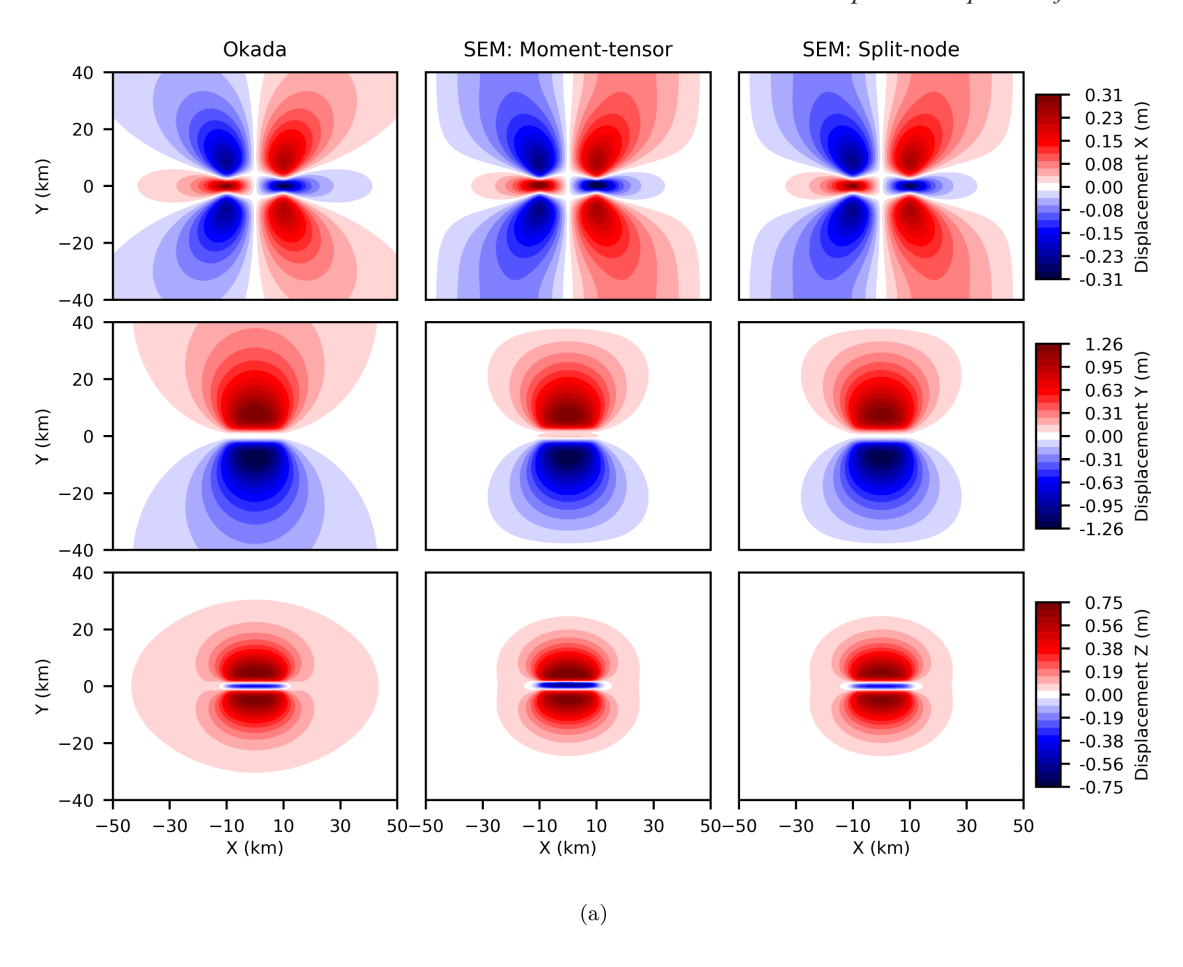


Figure 14. Displacement field computed with the SIEM on the free surface for the vertical strike-slip fault for different mesh refinements with the split-node approach. Rows top to bottom: *x*-, *y*-, and *z*-components. Columns left to right: element sizes 4, 2 and 1 km.



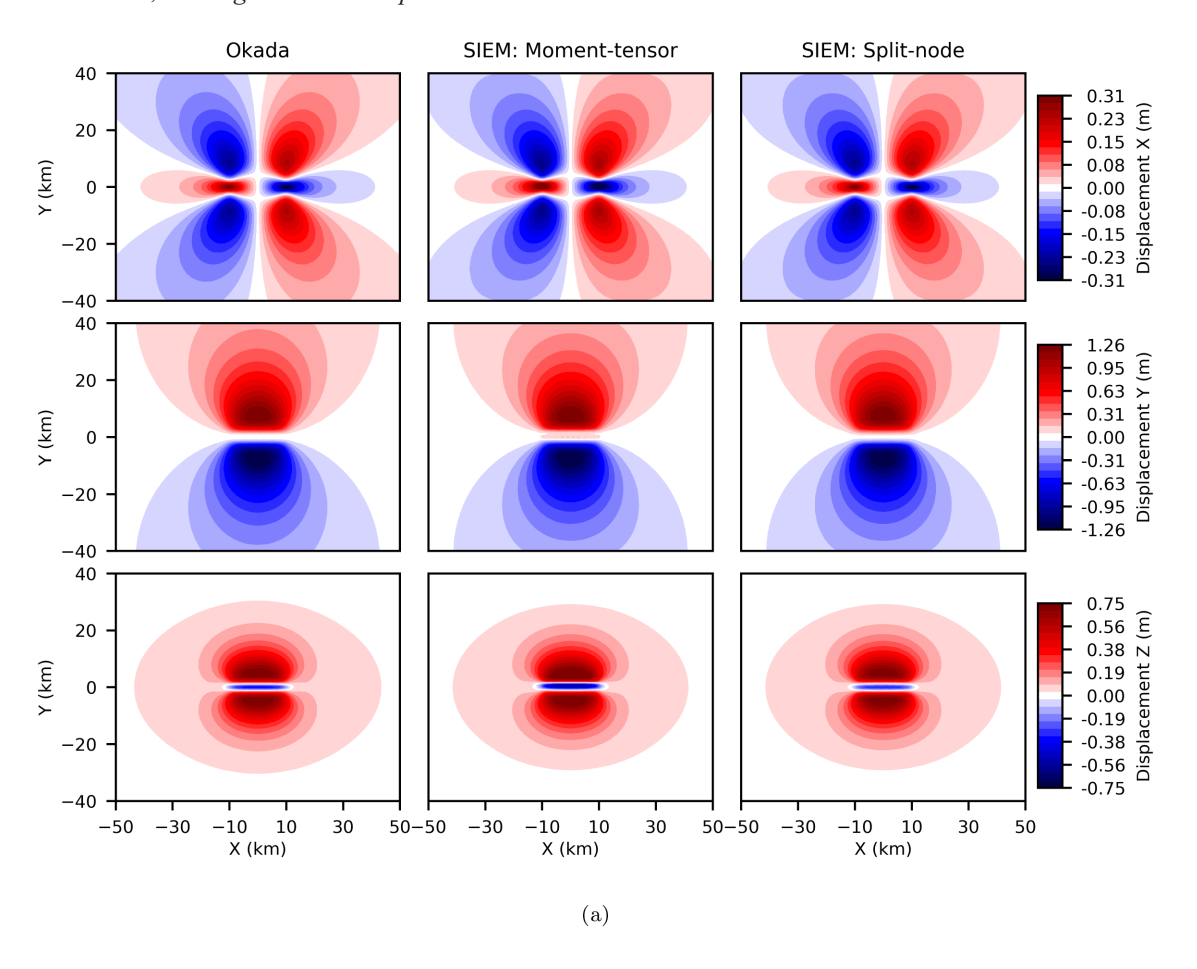
	Differences between SEM and Okada results			
(b)	Component	CMT solution	Split-node solution	
	X component	.284	.282	
	Y component	.283	.283	
	Z component	.777	.791	
	Total	.369	.369	

Figure 15. (a) Displacement field computed with the SEM on the free surface for the vertical tensile fault. Rows top to bottom: *x*-, *y*- and *z*-components. Columns left to right: Okada semi-analytical solution, SEM with moment-density tensor approach, and SEM with split-node approach. (b) Differences between the SEM and Okada results calculated with eq. (49).

Resulting snapshots for the displacement field on the top surface are shown in the Fig. 15. The numerical results for both the moment-density tensor and the split-node approaches are in good agreement with the Okada solution, although we observe discrepancies farther away from the source. Right at the fault, the node split approach is more accurate because it explicitly specifies the slip on the fault nodes. We observe some discrepancies for the moment-density tensor approach, which is not discontinuous on the fault surface. To take a closer look, we plot profiles along the y-axis at x = 0 km in Fig. 17 in the left-hand column.

For all components, the numerical results are generally in agreement with the Okada solution, and the split-node result is significantly better than the moment-density tensor result. Further away from the fault, all components exhibit significant discrepancies. Since the moment-density tensor approach does not exactly satisfy the slip condition on the fault, we observe some numerical discrepancies near the fault.

Next, for the same model, we add a single layer of infinite elements to impose Dirichlet boundary conditions at infinity. We perform simulations for both the moment-density tensor and the split-node approaches. Fig. 16 shows snapshots of the surface displacement field. Both numerical results are in excellent agreement with the Okada solution for all components, and the deformation pattern is correctly reproduced by both approaches. We still observe some numerical discrepancies for the moment-density tensor approach close to the fault. The right-hand



	Differences between SIEM and Okada results			
	Component	CMT SIEM	Split-node SIEM	
	X component	.063	.017	
(b)	Y component	.017	.015	
	Z component	.068	.050	
	Total	.032	.023	

Figure 16. (a) Displacement field computed with the SIEM on the free surface for the vertical tensile fault. Rows top to bottom: *x*-, *y*- and *z*-components. Columns left to right: Okada analytical solution, SIEM with moment-density tensor approach, and SIEM with split-node approach. (b) Differences between the SIEM and Okada results calculated with eq. (49).

column of Fig. 17 shows surface profiles along the *y*-axis. Addition of the infinite-element layer significantly improves the results for both approaches. We observe that the split-node approach is in excellent agreement with the Okada solution, including near the fault, but the moment-density tensor approach has not improved. This suggests that the moment-density tensor approach may not be suitable for near-field simulations.

4.1.3 Inclined fault

In this example, we consider the same model domain as in the previous examples. The fault has the same size and location, but dips at a 45° angle, as shown in Fig. 18. To honour the fault surface, we cut the entire model through the fault plane. First, to asses the effects of mesh quality, we intentionally create a mesh that has poor-quality elements around the fault region, as shown in Fig. 19. For example, the distortion metric of the elements on the fault surface is low as 0.46. We use an average element size of 2 km. The mesh consists of 52 900 elements, 441 269 points, and 1 323 807 degrees of freedom.

We perform simulations with both the moment-density tensor and split-node approaches. Resulting snapshots of the displacement fields

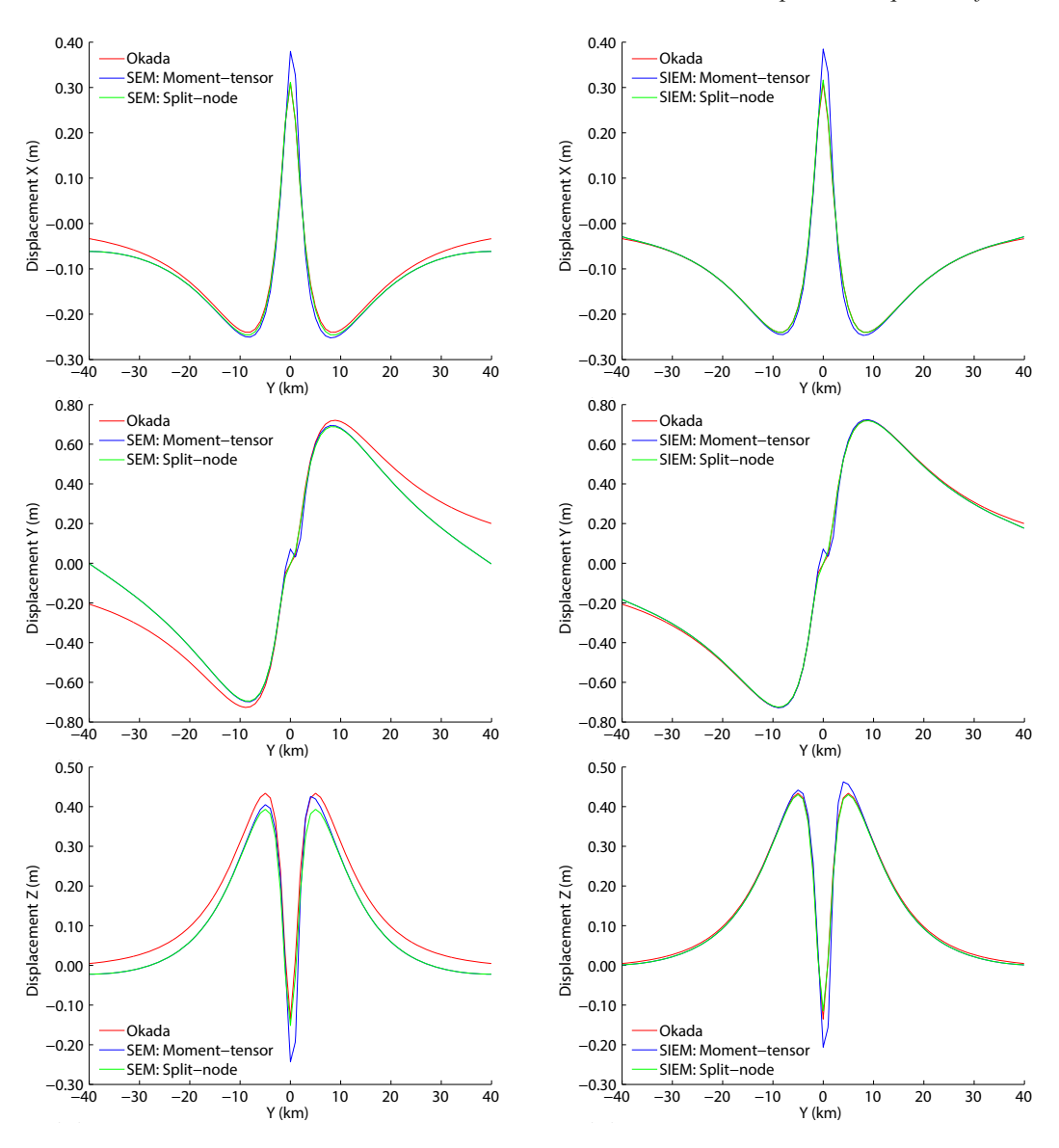


Figure 17. Profiles of the the displacement field plotted along y-axis at x = -10 km on the top surface for the vertical tensile fault. Top to bottom rows are x-, y- and z-components, respectively. Left-hand column: SEM. Right-hand column: SIEM.

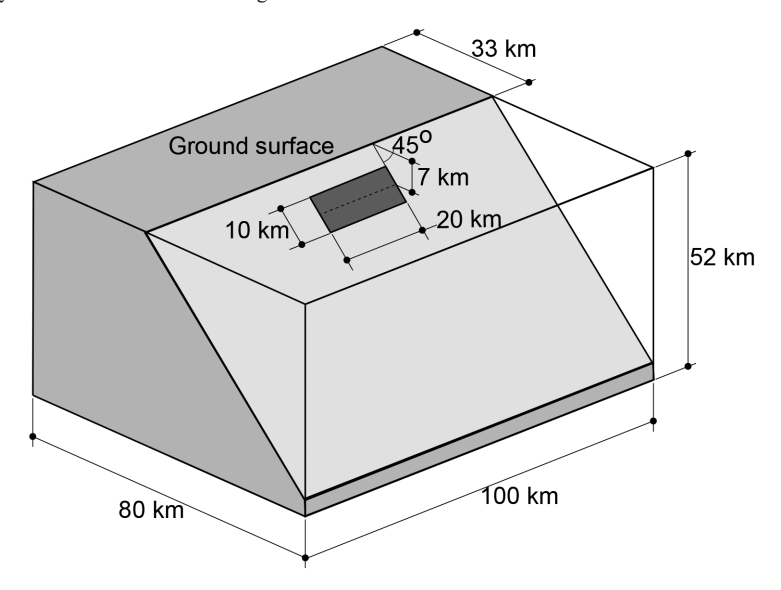


Figure 18. Model geometry of the inclined fault. The model is cut through the fault plane so that the fault is visible. The fault surface is shown in dark grey.

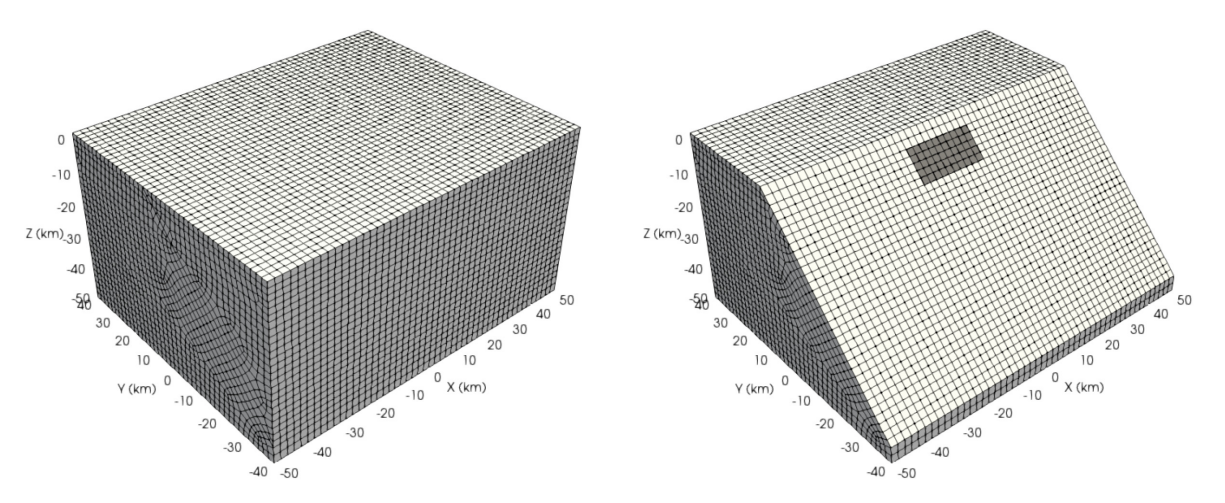


Figure 19. Left-hand panel: spectral-element mesh of an inclined fault model. Smallest value of distortion metric of the elements on the fault surface is 0.46 indicating a poor-quality mesh. Right-hand panel: the model is cut through the fault plane to reveal the fault. The fault surface is shown in dark grey.

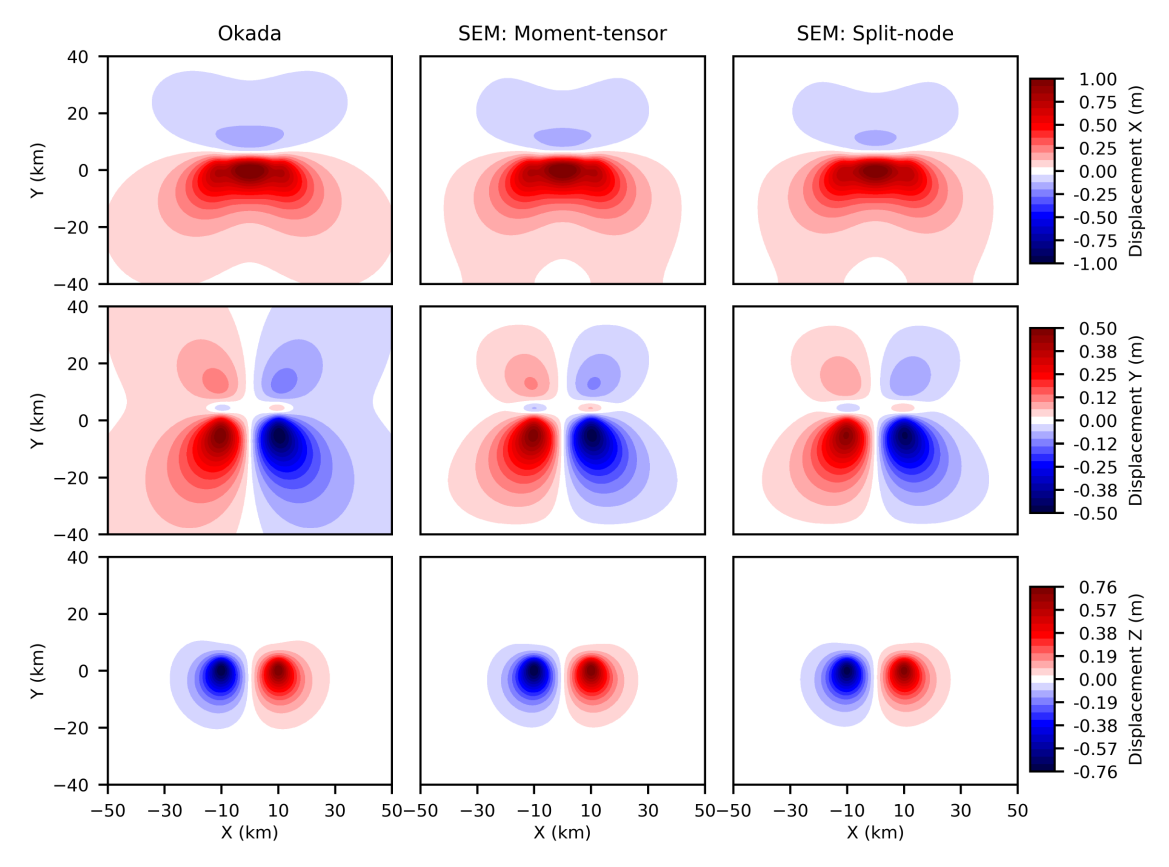


Figure 20. Displacement field computed with the SEM on the free surface for the inclined fault. Rows top to bottom: x-, y- and z-components. Columns left to right: Okada analytical solution, SEM with moment-density tensor approach, and SEM with split-node approach.

computed on the free surface are shown in Fig. 20. Both numerical results are in good agreement with the analytical solution. Both methods are capable of reproducing the major features of the deformation pattern, although we observe some discrepancies, in particular for the *x*-and *y*-components. Another interesting observation is that, for this example, the split-node result is actually worse than the moment-density tensor result. For closer inspection, we plot profiles for each component on the free surface along the *x*-axis, as shown in the left column of Fig. 22. We observe significant discrepancies, particularly for the *y*-component. We clearly observe that the moment-density tensor result is better than the split-node result, even near the fault.

We add the infinite-element layer outside the model domain and impose Dirichlet boundary conditions at infinity. The total number of infinite elements is 6816—approximately 13 per cent of the original number of elements. Again, we perform simulations with both the moment-density tensor and the split-node approaches. Resulting snapshots of the displacement field on the top surface are shown in Fig. 21. Profiles for each component are plotted along the *x*-axis at y = 0 km are shown in Fig. 22 in the right-hand column. The results are notably

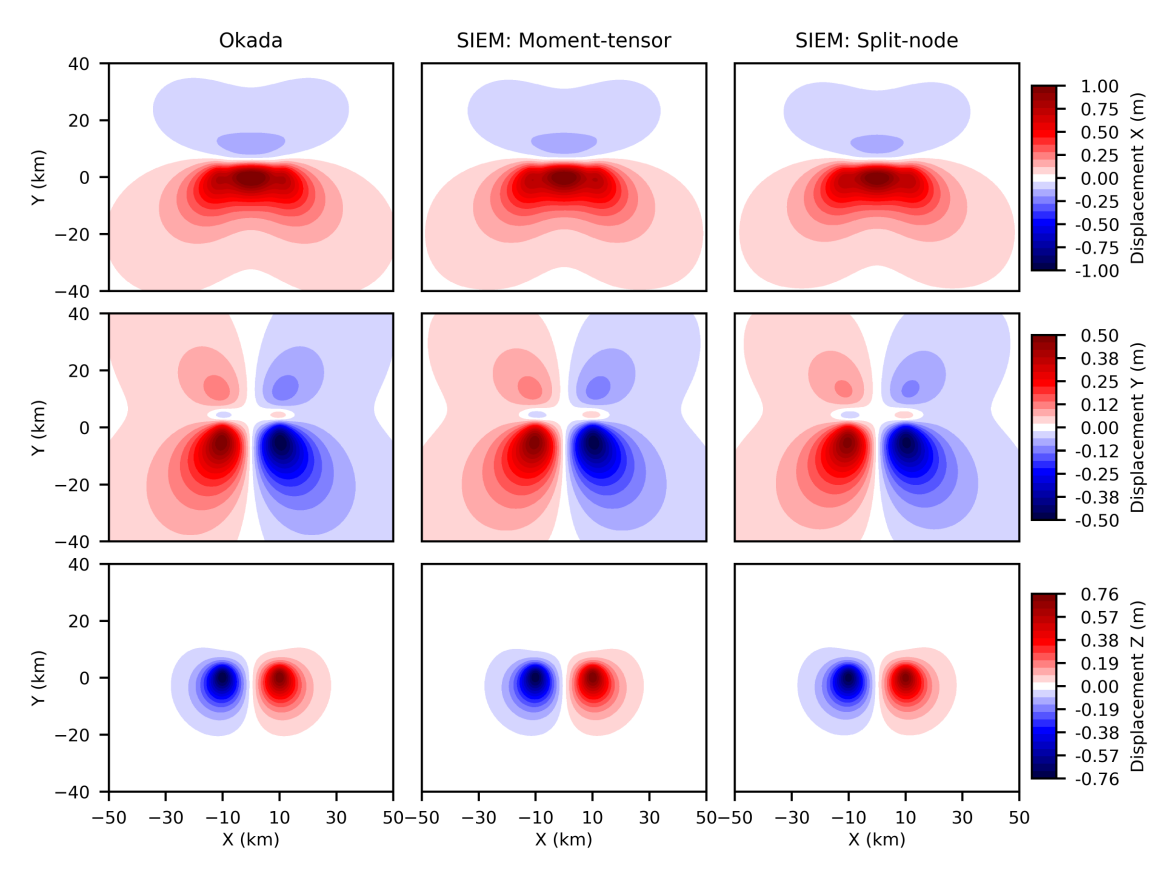


Figure 21. Displacement field computed with the SIEM on the free surface for the inclined fault. Rows top to bottom: *x*-, *y*- and *z*-components. Columns left to right: Okada analytical solution, SIEM with moment-density tensor approach, and SIEM with split-node approach.

better for all components, especially near the boundary. We again observe that the moment-density tensor results are better than the split-node results near the fault.

In an attempt to improve the simulations, we remesh the model with high-quality hexahedra around the fault, as shown in Fig. 23. The distortion metric of the elements on the fault surface is improved from 0.46 to 1.0. We use the same element size of 2 km. The mesh consists of 53 400 elements, 445 107 points, and 1 335 321 degrees of freedom. We plot snapshots of the displacement fields on the free surface, as shown in Fig. 24. Profiles for each component along the *x*-axis at y = 0 km on the free surface are shown in the left column of Fig. 26. The numerical results are much improved compared to the low-quality mesh. Displacement patterns for all components are accurately reproduced, although we observe the some discrepancies for the *y*-component. Both the moment-density tensor and the split-node approaches give very good results.

Next, we add the infinite-element layer and impose Dirichlet boundary conditions at infinity. Specifically, 6736 additional elements are created. Resulting snapshots for the displacement field computed on the free surface are shown in Fig. 25, and profiles for each displacement component along the x-axis at y = 0 are shown in Fig. 26 on the right. Both numerical results are now in excellent agreement with the Okada solution. The y-component results are significantly improved for both approaches. Displacement patterns are accurately reproduced both near and further from the source.

The last two examples with different quality meshes demonstrate that it is important to have a high-quality mesh around the fault for the split-node approach. It is of course always important to have a high-quality mesh, but some times it is difficult to obtain such a high-quality mesh due to complexity of the model geometry. If the mesh around the fault is of poor quality, the moment-density tensor approach may be the better option.

4.2 Viscoelastic benchmarks

In the following examples, we simulate the viscoelastic response and compare the results with the analytical solution for an axial loading and semi-infinite strike-slip fault, and a finite-element solution for an earthquake source. We set the zero initial conditions for all examples. Although the axial loading example is not directly related to the coseismic and post-earthquake deformation, it serves as the demonstration of the accuracy of implementation of the viscoelastic rheologies. Further, it demonstrates the applicability of our package not only to the seismic sources but also to other loading.

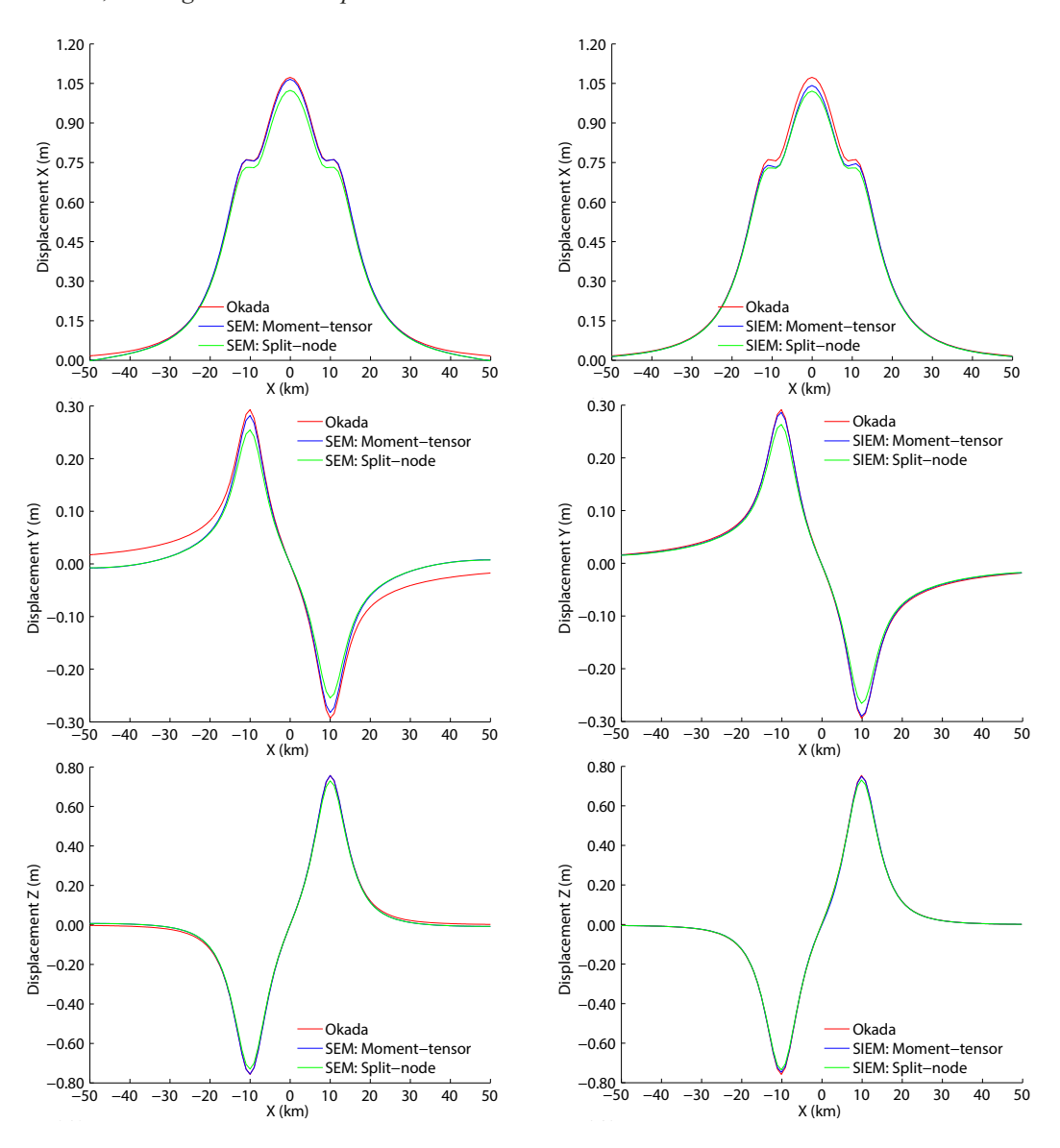


Figure 22. Profiles of the displacement field plotted along x-axis at y = 0 km on the top ground surface for the inclined fault. Top to bottom rows are x-, y- and z-components, respectively. Left-hand column: SEM. Right-hand column: SIEM.

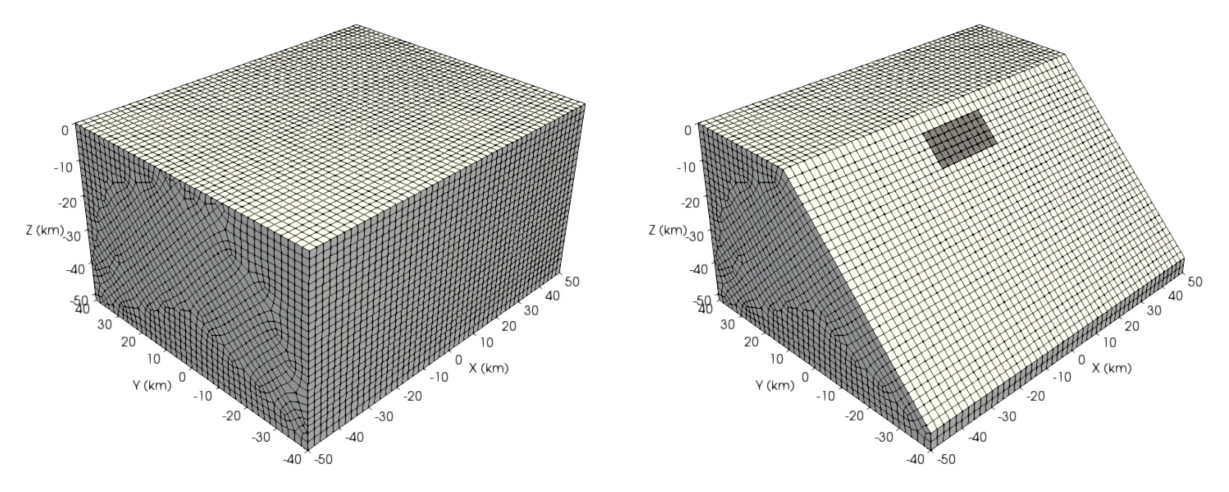


Figure 23. Left-hand panel: Higher-quality spectral-element mesh of an inclined fault model. All elements on the fault surface has a distortion metric 1.0 indicating a high-quality mesh. Right-hand panel: The model is cut through the fault plane to visualize the fault. The fault surface is shown in dark gray.

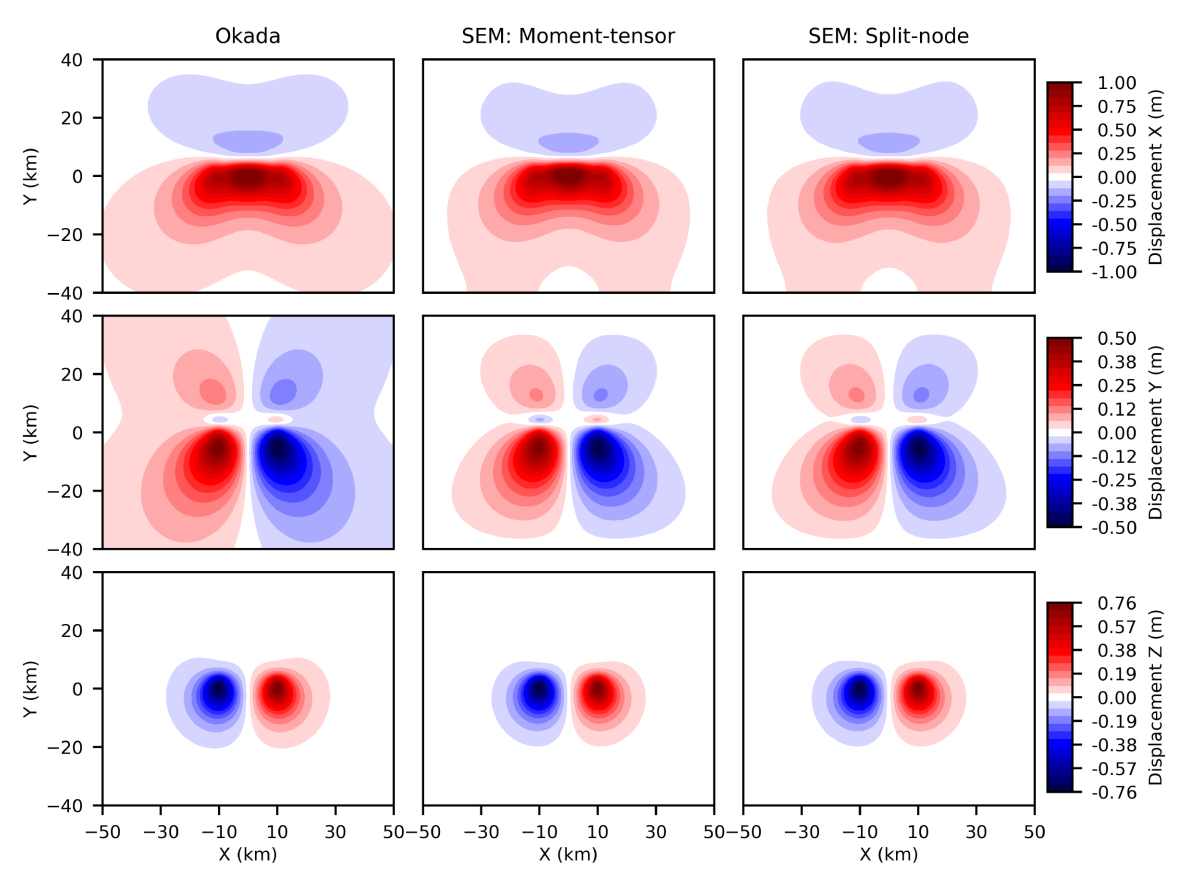


Figure 24. Displacement field computed with the SEM on the free surface for the inclined fault using a high-quality mesh. Rows top to bottom: *x*-, *y*- and *z*-components. Columns left to right: Okada analytical solution, SEM with moment-density tensor approach, and SEM with split-node approach.

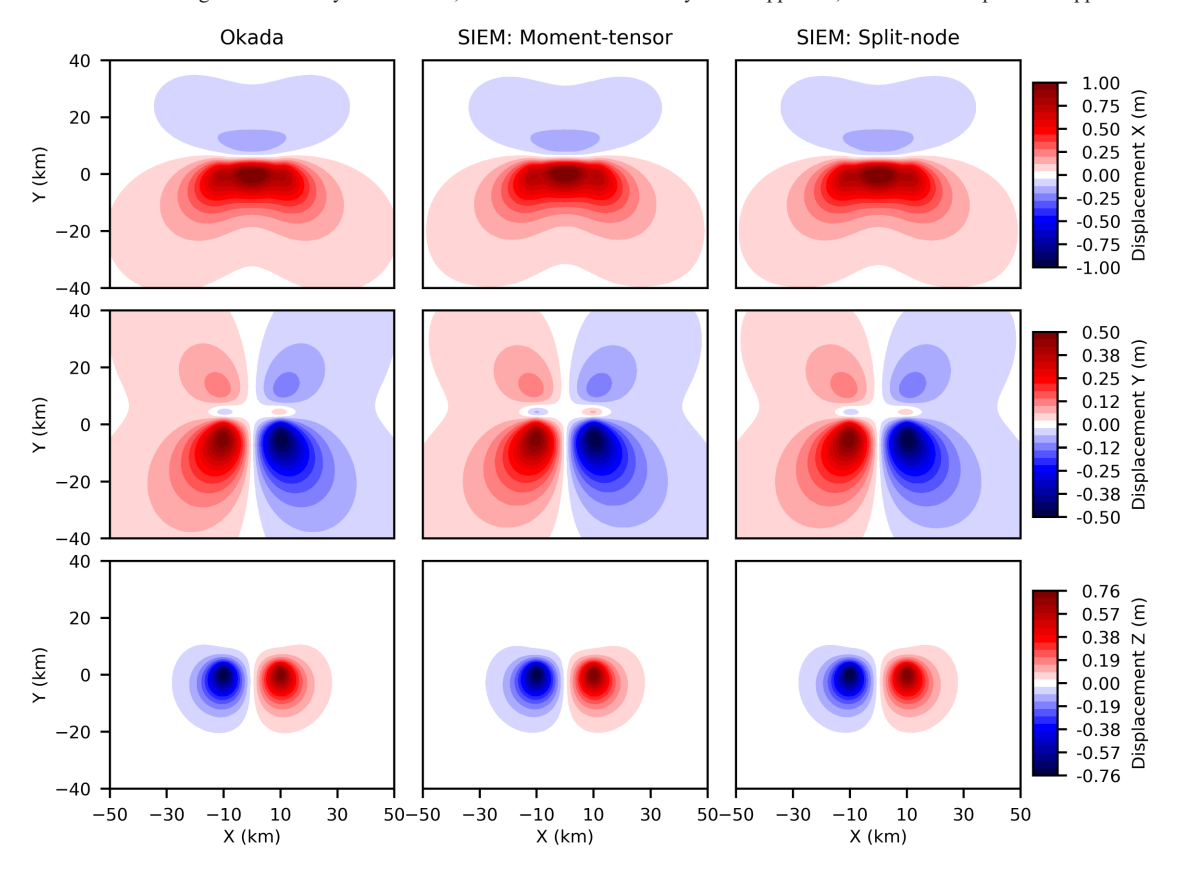


Figure 25. Displacement field computed with the SIEM on the free surface for the inclined fault using a high-quality mesh. Rows top to bottom: *x*-, *y*-, and *z*-components. Columns left to right: Okada analytical solution, SIEM with moment-density tensor approach, and SIEM with split-node approach.

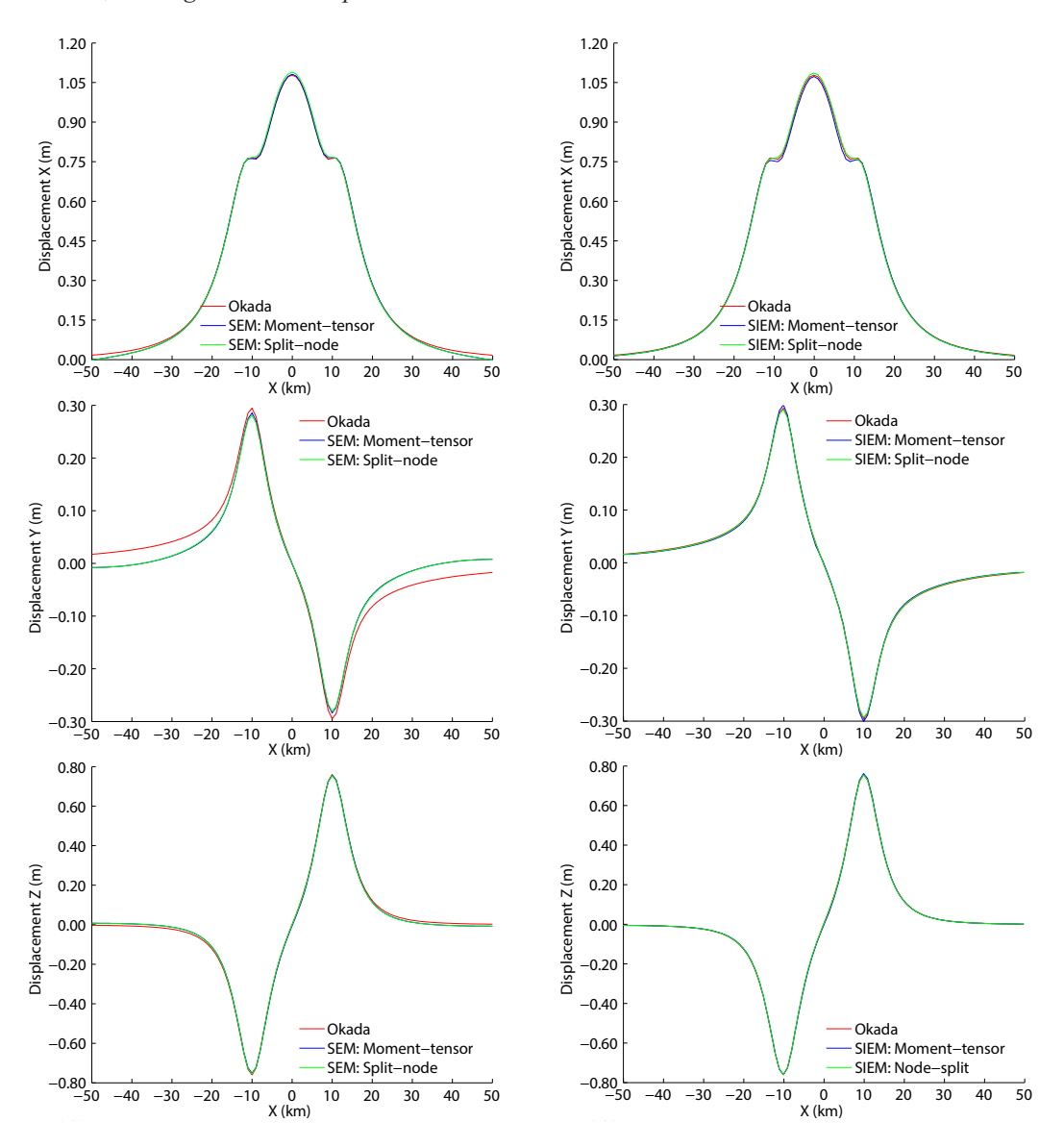


Figure 26. Profiles of the the displacement field plotted along x-axis at y = 0 km on the top surface for the inclined fault using a high-quality mesh. Top to bottom rows are x-, y-, and z-components, respectively. Left-hand column: SEM. Right-hand column: SIEM.

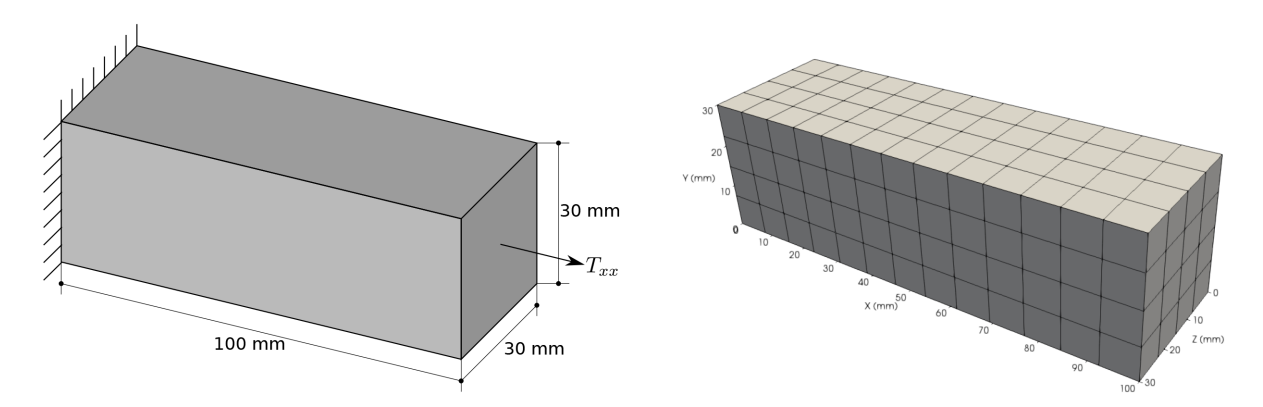


Figure 27. Left-hand panel: A cantilever rod under an axial stress. Right-hand panel: Mesh for the cantilever rod. Axial stress $T_{xx}=10$ MPa.

4.2.1 Cantilever rod under axial stress

In order to verify the implementation of a viscoelastic rheology, we first simulate the viscoelastic response of a rod with a square cross section $30 \text{ mm} \times 30 \text{ mm}$ and a length 100 mm, as shown in Fig. 27a. The rod has Young's modulus = 1000 MPa, Poisson's ratio 0.4833, and

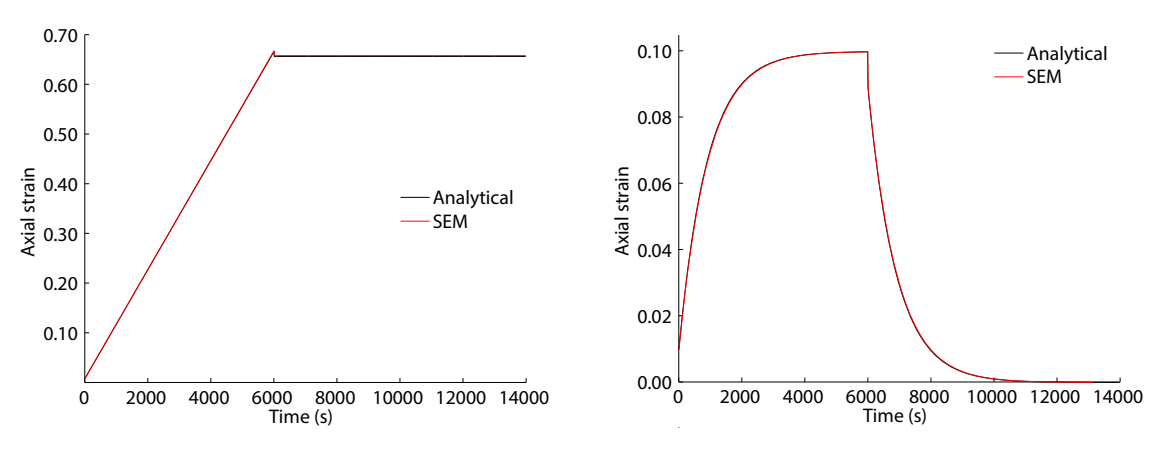


Figure 28. Viscoelastic response for the rod. Left-hand panel: Maxwell rheology. Right-hand panel: Standard linear solid, i.e., a general Maxwell rheology with a single Maxwell element.

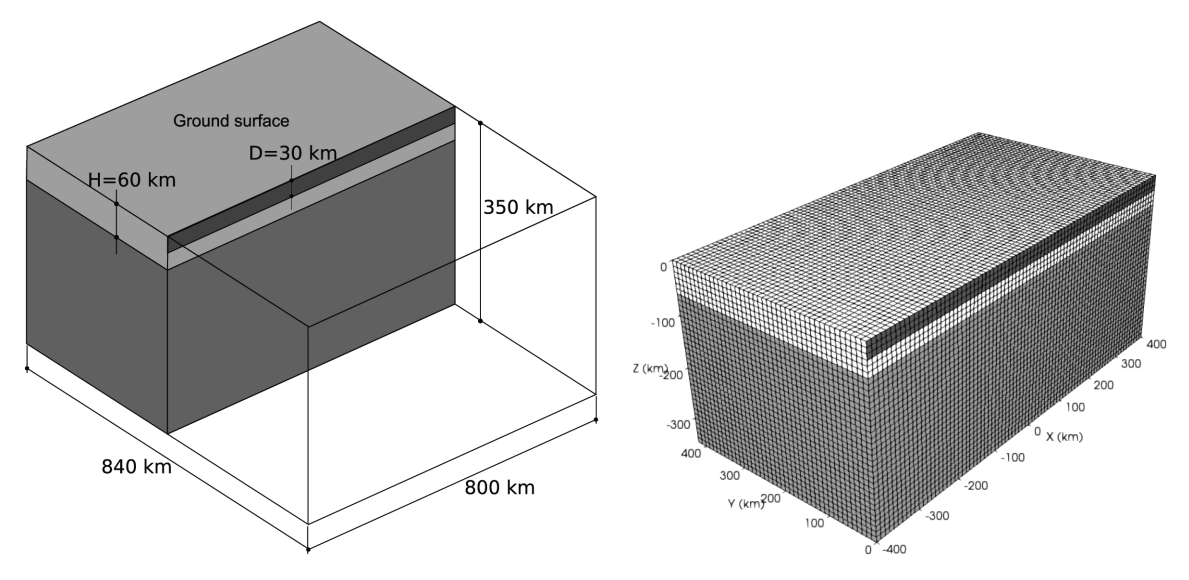


Figure 29. Left-hand panel: Model geometry for the semi-infinite vertical strike-slip fault. Right-hand panel: Spectral-element mesh for the semi-infinite vertical strike-slip fault. The fault surface is shown in dark gray. An elastic layer (light gray) is overlying a viscoelastic layer (gray).

viscosity 9×10^{10} Pa s. This particular example may be found in Marques & Creus (2012). We mesh the model using hexahedral elements resulting in a total of 208 spectral elements. Elements have an average cross-section 7.5 mm \times 7.5 mm and are \approx 7.7 mm long. We perform two simulations with a Maxwell rheology and a standard linear solid or a Zener model. The shear modulus of the Maxwell element in the general Maxwell rheology is determined by the moduli ratio $r^1 = 0.901$. The left end of the rod is fixed. An axial stress $T_{xx} = 10$ MPa is instantly applied at the right end of the rod and held constant until 6000 s, at which point the stress is released. We set the time step to 10 s for the simulations. We plot the time series of the axial strain observed at the right end of the rod (Fig. 28). We obtain an excellent match for both rheologies.

4.2.2 Semi-infinite vertical strike-slip fault

In this example, we construct a semi-infinite strike-slip fault model with dimensions $800 \,\mathrm{km} \times 840 \,\mathrm{km} \times 350 \,\mathrm{km}$, as shown in Fig. 29. The elastic layer has a thickness $H = 60 \,\mathrm{km}$ and overlies a viscoelastic layer with a thickness of 290 km with a Maxwell rheology. The fault surface extends to a depth $D = 30 \,\mathrm{km}$ in the elastic layer, such that the ratio D/H = 0.5. For this model Nur & Mavko (1974) derived an analytical solution, and Savage & Prescott (1978) generalized this solution for a number of earthquake cycles.

We use a shear modulus $\mu = 4.439663 \times 10^{10}$ N m⁻² and viscosity $\eta = 7.00046 \times 10^{19}$ Pa s, such that the characteristic time is $2 \eta/\mu = 100.0$ yr. We set Poisson's ratio to 0.25. We consider a single earthquake cycle with a uniform slip rate of $2 \Delta \dot{\mathbf{s}} = 0.04$ m yr⁻¹ along strike for T = 100 yr, for a total slip $\Delta \mathbf{s} = 2 \Delta \dot{\mathbf{s}} T = 4$ m.

We mesh the model using hexahedral elements of dimension 10 km. The mesh consists of 235 200 spectral elements and 1 931 839 nodes resulting in a total of 5 721 590 degrees of freedom. We impose a traction free boundary condition on the top surface, and vanishing Dirichlet boundary conditions on the lateral and bottom surfaces. We set a time step of 10 yr and run the simulation for 100 yr, which takes \approx 9 min on 80 processors.

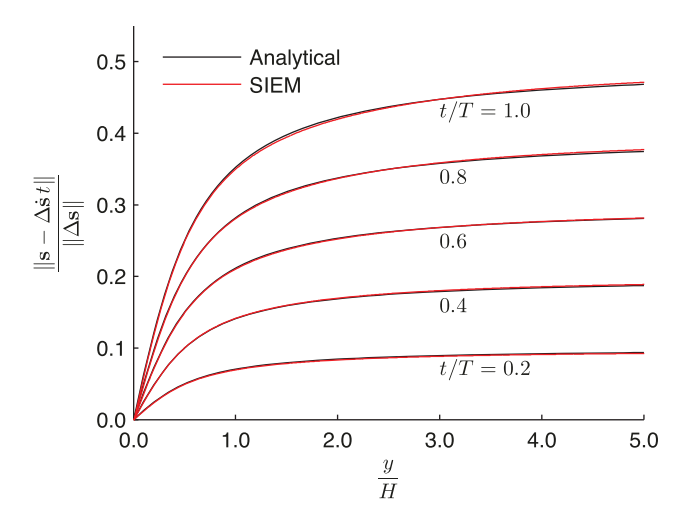


Figure 30. Ratio of surface displacement to coseismic slip, $\|\mathbf{s} - \Delta \dot{\mathbf{s}} t\| / \|\Delta \mathbf{s}\|$, as a function of the ratio of the perpendicular distance from the fault to the thickness of the elastic layer, v/H, computed for various time ratios for a semi-infinite strike-slip fault.

We plot the ratio of surface displacement to coseismic slip as a function of the ratio of perpendicular distance from the fault to the thickness of the elastic layer for time ratios $t/T=0.2,\ 0.4,\ 0.6,\ 0.8$ and 1.0, which correspond to times of 20, 40, 60, 80 and 100 yr, respectively, as shown in Fig. 30. In order to match the results with the analytical solution given by Savage & Prescott (1978), surface displacement at a given time is computed by subtracting the coseismic slip, $\Delta \hat{s} t$, from the total displacement, s, at that time. The numerical results are in excellent agreement with the analytical solutions for all time ratios.

4.2.3 PyLith example

PyLith is a FEM package that can simulate dynamic and quasi-static seismic processes. This code is available from the Computational Infrastructure for Geodynamics (CIG) website and is widely used to simulate coseismic deformation, post-earthquake relaxation and dynamic rupture (Hsu et al. 2011; Douilly et al. 2015). It uses a first-order spatial discretization, so mesh elements must be quite small, especially in the vicinity of the fault, in order to guarantee accuracy. PyLith can simulate post-earthquake relaxation using a variety of viscoelastic rheological models. We performed coseismic (elastic) and post-earthquake (viscoelastic) benchmarks with PyLith 2.2.0 (Aagaard et al. 2013a,b). These benchmarks demonstrate that our method can match the accuracy of an existing FEM package for coseismic and post-earthquake simulations.

Because PyLith requires very small elements near the fault, we designed different meshes for our SEM and PyLith simulations. For the PyLith simulations, we used a modified version of the mesh from PyLith's own Savage & Prescott benchmark in Aagaard *et al.* (2013a). The mesh has hexahedral elements that are 20 km long. A box measuring $640 \text{ km} \times 400 \text{ km} \times 140 \text{ km}$ in the center of the mesh has refined elements 6.7 km long. The total mesh dimensions are $2,000 \text{ km} \times 1,000 \text{ km} \times 400 \text{ km}$. For the SEM simulations, we used a mesh with 13.3 km mesh spacing throughout the domain. Our SEM simulation has 3 GLL points per element side, meaning that it is second order, so this choice of mesh spacing yields the same nodal spacing as the PyLith mesh around the fault. Both simulations have homogeneous material properties with Young's modulus $5.68 \times 10^{10} \text{ N m}^{-2}$ and Poisson's ratio 0.26. For the viscoleastic simulations, the lower 280 km of the domain has a Maxwell viscoelastic rheology with $\eta = 7.1 \times 10^{19} \text{ Pa}$ s. A diagram of the model domain is shown in Fig. 31.

For this benchmark, we used a vertical strike-slip fault running along the *y*-axis of the domain. It is 213 km long and 53 km wide, centered at 47 km depth. We imposed uniform slip of 2 meters. PyLith implements the earthquake source via split-nodes, so we use our split-node implementation for this benchmark. PyLith faults have slip that tapers linearly over the edge elements of the fault so that it goes to zero at the nodes that form the fault's edges. Our SEM code can accommodate both tapered and non-tapered split-node faults, and we compare both results to the PyLith output. We use the built-in tapering option to implement the taper.

The two meshes for this benchmark are shown in Fig. 32. The SEM mesh, shown in Fig. 32a, has a total of 353 400 elements and 383 691 nodes. It honours the fault surface. The PyLith mesh has 252 105 elements and 260 696 nodes. This mesh also honours the fault surface, but the dimensions of the fault are specified by selecting the nodes that comprise the fault.

The boundary conditions for this benchmark are identical to those used for the non infinite-element Okada simulations: the top surface has a traction-free boundary condition, and Dirichlet boundary conditions are imposed on the lateral and bottom surfaces. It is not necessary to use infinite elements for the PyLith simulations because it is possible to impose the same boundary conditions on the PyLith and SEM simulations. PyLith does not currently support far-field boundary conditions.

First we performed an elastic (coseismic) benchmark. Fig. 33 shows displacement profiles for all three simulations. These profiles show y-component surface displacement on a line perpendicular to the fault. The tapered SEM displacement solution is close to the PyLith result. The non-tapered SEM solution has a similar shape to the tapered solution, but as expected it is larger because there is more net slip on the fault. Fig. 34 shows the surface displacement field for these three simulations.

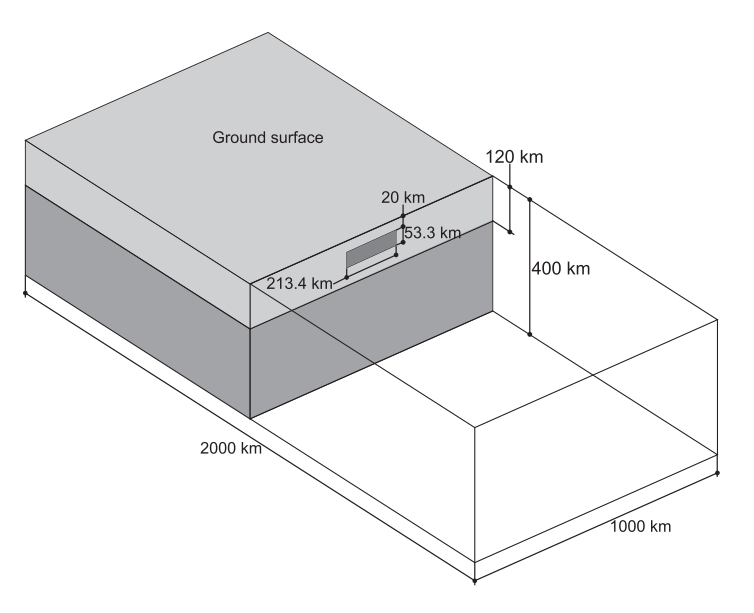


Figure 31. Model domain for the Pylith benchmark. The model consists of an upper elastic layer (light gray) and a lower viscous layer (dark gray). The model has been cut along the fault plane so that the fault is visible at the center of the model.

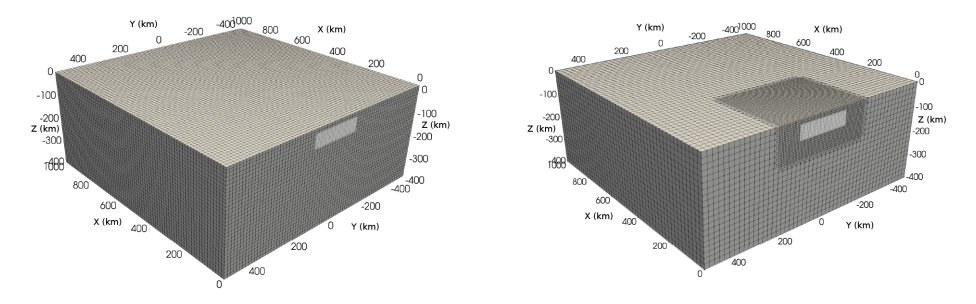


Figure 32. Left-hand panel: spectral-element mesh for the PyLith benchmark. The model has been cut along the *y*-axis so that the fault surface is visible as a white rectangle. Right-hand panel: PyLith mesh for the benchmark. Note the smaller elements at the center of the mesh.

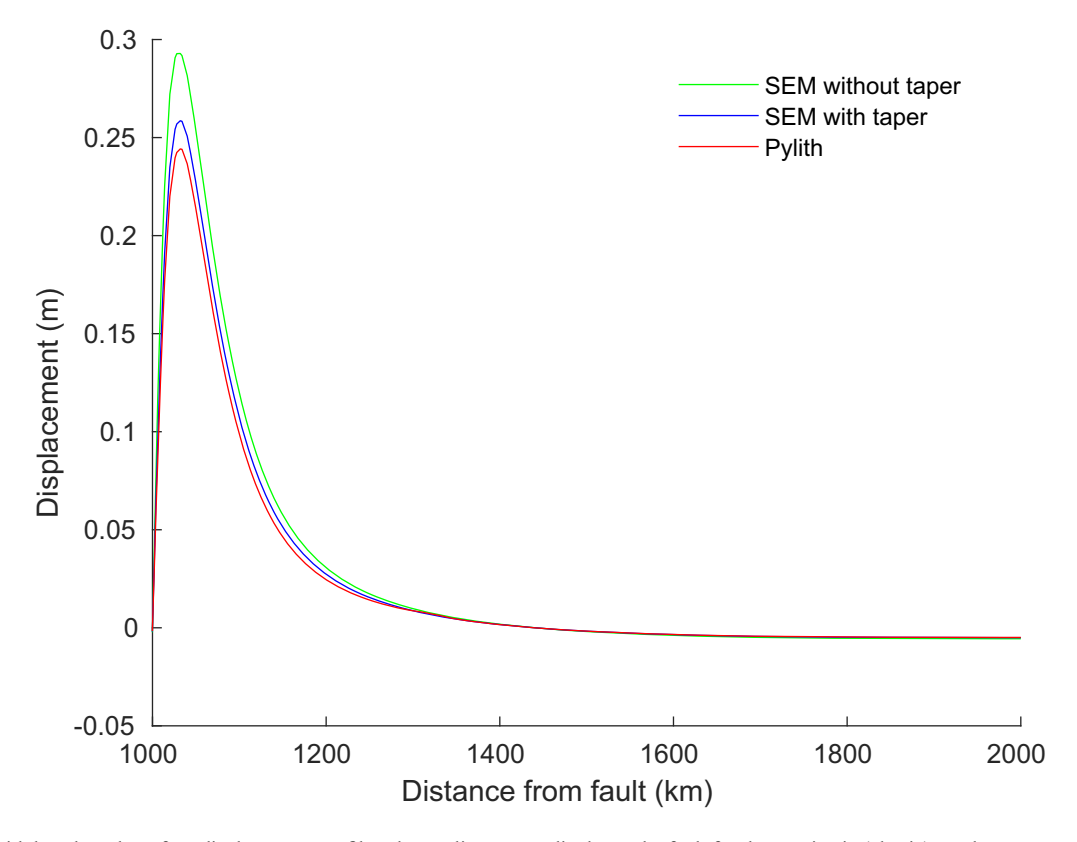


Figure 33. PyLith benchmark surface displacement profiles along a line perpendicular to the fault for the coseismic (elastic) result.

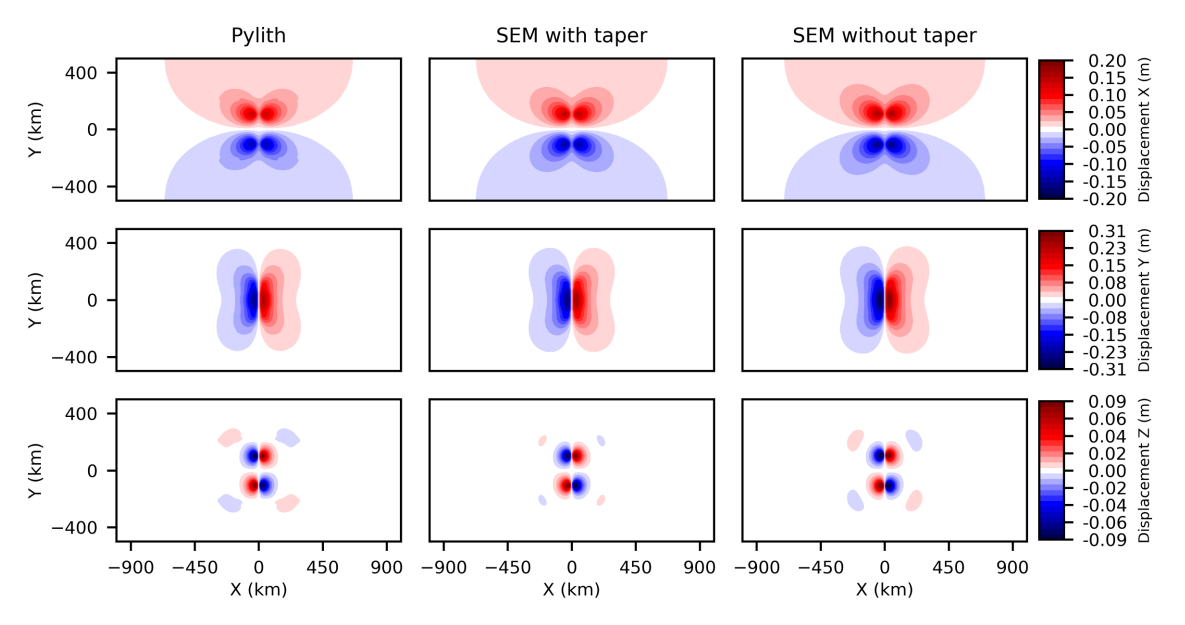


Figure 34. PyLith benchmark surface displacement field for the coseismic (elastic) result. Rows top to bottom: *x*-, *y*- and *z*-components. Columns left to right: Pylith solution, SEM solution for a tapered fault and SEM solution for a non-tapered fault.

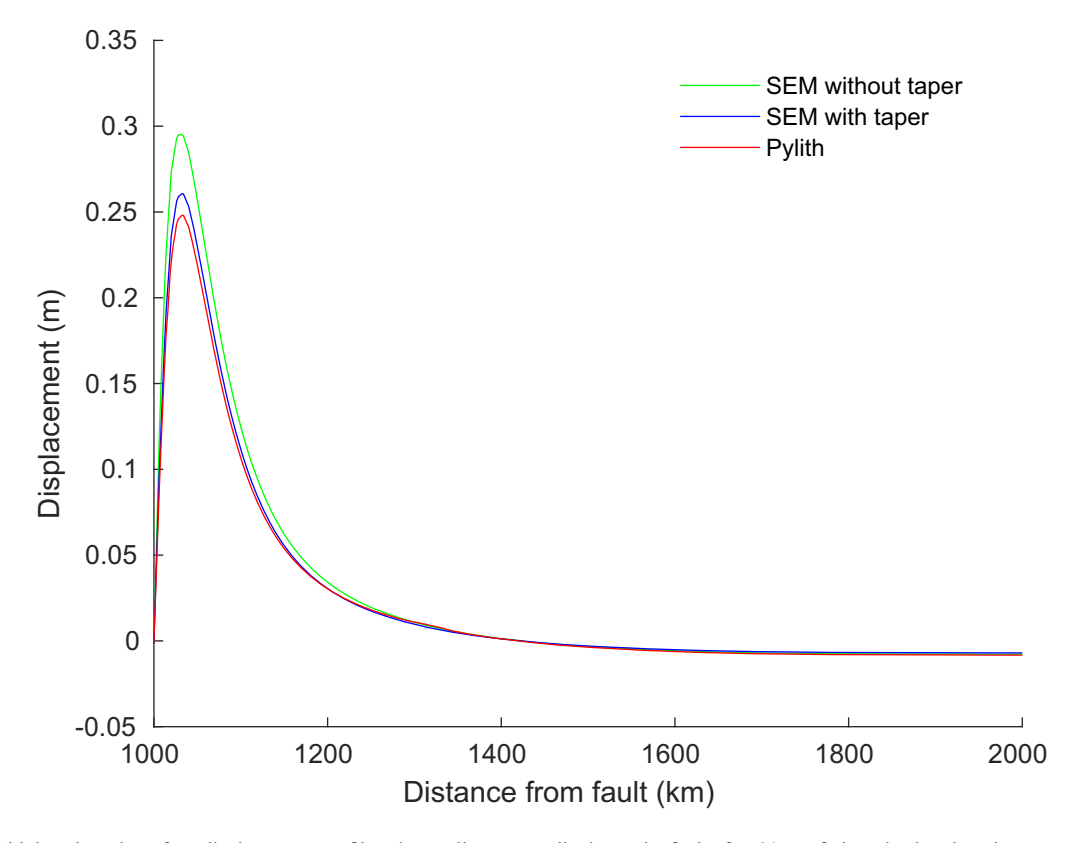


Figure 35. PyLith benchmark surface displacement profiles along a line perpendicular to the fault after 90 yr of viscoelastic relaxation.

Then we allowed the model to relax viscoelastically and plotted the profiles and surface displacement fields after 90 yr. These results are shown in Figs 35 and 36. The tapered and non-tapered SEM solutions have a similar shape to the Pylith result and have experienced a similar amount of relaxation after 90 yr. Fig. 37 shows the rate of relaxation for a point on the surface of the mesh. Note that the Maxwell relaxation time is approximately 39.6 yr.

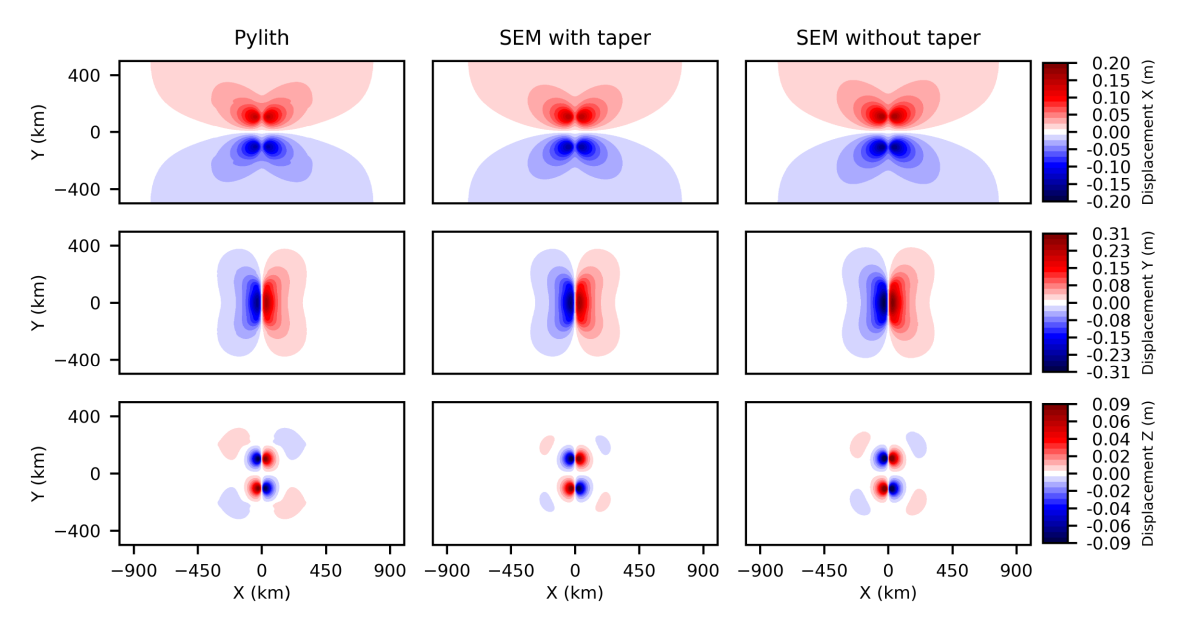


Figure 36. PyLith benchmark surface displacement field for a Maxwell viscoelastic rheology. Results are shown after 90 yr of relaxation. Rows top to bottom: x-, y- and z-components. Columns left to right: Pylith solution, SEM solution for a tapered fault, and SEM solution for a non-tapered fault.

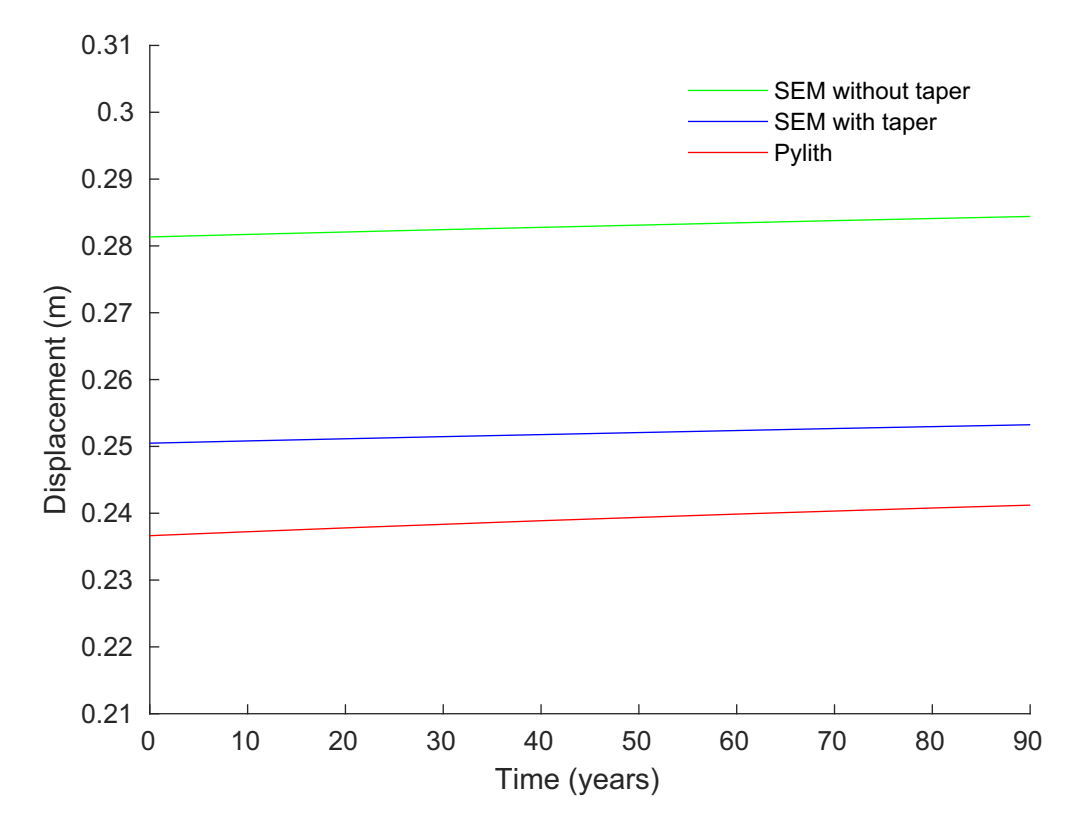


Figure 37. Rate of relaxation from 0 to 90 yr for y-component of displacement at a point on the surface of the Pylith and SEM meshes.

5 DISCUSSION

We successfully implemented a SIEM for 3-D coseismic and post-earthquake deformation problems using moment-density tensor and split-node approaches for the source implementation. We observed excellent agreement between the SIEM results and corresponding analytical solutions for both coseismic and post-earthquake deformation. Implementation of the moment-density tensor and split-node approaches allows us to accommodate complex fault models. The moment-density tensor approach is easy to implement, but it may not be accurate at or near the fault for a tensile source. This is due to the fact that the moment-density tensor approach generates a continuous force field and is therefore unable to capture the tensile or opening discontinuity accurately. This problem may be alleviated by using a finer mesh around the fault. The split-node implementation is more accurate, but its performance depends on the mesh quality around the fault. The moment-density

tensor approach may be a better option in situations where it is difficult to create a high-quality mesh that honours the fault surface. Infinite elements significantly improve the results while adding insignificant memory and computational costs. Although we have not specifically used adaptive mesh refinement—that is, *h*-refinement—in our examples, accuracy and efficiency can be significantly improved by adding infinite elements on top of an adaptively refined mesh. Since infinite-elements can be generated by just sweeping surface elements along the infinite direction, the SIEM can be applied to very complex models, including those with realistic topography.

For viscoelastic problems, it is generally known that lower order isoparametric elements suffer from the so-called shear locking phenomenon, which can be alleviated by using reduced integration and/or higher-order Lagrangian elements (Simo & Hughes 1998; Zienkiewicz & Taylor 2005). It will be of interest to explore how the SIEM behaves for such problems.

In a complementary study (Langer *et al.* 2018), we investigate the effects of 3-D heterogeneous material properties and realistic topography on coseismic and post-earthquake deformation. Infinite-elements naturally couple with spectral-elements, which allows us to solve coupled elastic-gravitational problems efficiently. Future work will focus on applications to challenging global quasi-static and dynamic problems, such as earthquake-induced gravity perturbations, tsunamis and glacial rebound.

Our package is open-source and freely available via the Computational Infrastructure for Geodynamics (geodynamics.org).

ACKNOWLEDGEMENTS

We thank Carl Tape and Michael Bevis for helpful discussions, Brad Aagaard for advice with the PyLith benchmark, and Stefano Zampini for his help with implementing the PETSc library. Parallel programs were run on computers provided by the Princeton Institute for Computational Science and Engineering (PICSciE). 3-D data were visualized using the open-source parallel visualization software ParaView/VTK (www.paraview.org). 2-D snapshots were created using the open-source Python plotting library Matplotlib (www.matplotlib.org). Most of the model sketches were created using the open-source vector graphics editor Inkscape (inkscape.org). An open-source copy of PyLith was downloaded from the Computational Infrastructure for Geodynamics (geodynamics.org) web site for benchmarking. We thank Brad Aagaard, an anonymous reviewer, and editor Carl Tape for insightful comments that helped to improve the manuscript.

REFERENCES

- Aagaard, B., Kientz, S., Knepley, M., Strand, L. & Williams, C., 2013b.
 PyLith User Manual, Version 2.2.0, Computational Infrastructure of Geodynamics. Davis. CA.
- Aagaard, B.T., Hall, J.F. & Heaton, T.H., 2001. Characterization of near-source ground motions with earthquake simulations, *Earthquake Spectra*, 17(2), 177–207.
- Aagaard, B.T., Knepley, M.G. & Williams, C.A., 2013a. A domain decomposition approach to implementing fault slip in finite-element models of quasi-static and dynamic crustal deformation, *J. geophys. Res.: Solid Earth*, 118(6), 3059–3079.
- Abdel-Fattah, T.T., Hodhod, H.A. & Akl, A.Y., 2000. A novel formulation of infinite elements for static analysis, *Comput. Struct.*, 77(4), 371–379.
- Agata, R., Ichimura, T., Hori, T., Hirahara, K., Hashimoto, C. & Hori, M., 2018. An adjoint-based simultaneous estimation method of the asthenosphere's viscosity and afterslip using a fast and scalable finite-element adjoint solver, *J. geophys. Int.*, 213(1), 461–474.
- Aki, K. & Richards, P.G., 2002. Quantitative Seismology, 2nd edn, University Science Books.
- Angelov, T.A., 1991. Infinite elements—theory and applications, *Comput. Struct.*, 41(5), 959–962.
- Balay, S. *et al.*, 2015. PETSc users manual, Tech. Rep. ANL-95/11 Revision 3.6, Argonne National Laboratory.
- Barbot, S. & Fialko, Y., 2010. A unified continuum representation of postseismic relaxation mechanisms: semi-analytic models of afterslip, poroelastic rebound and viscoelastic flow, J. geophys. Int., 182(3), 1124–1140.
- Beer, G. & Meek, J.L., 1981. 'Infinite domain' elements, *Int. J. Numer. Method Eng.*, 17(1), 43–52.
- Bettess, P., 1977. Infinite elements, Int. J. Numer. Method. Eng., 11(1), 53–64.
- Canuto, C., Hussaini, M.Y., Quarteroni, A. & Zang, T.A., 1988. Spectral Methods in Fluid Dynamics, Springer.
- Crawford, O., Al-Attar, D., Tromp, J. & Mitrovica, J.X., 2017. Forward and inverse modelling of post-seismic deformation, *J. geophys. Int.*, 208(2), 845–876.
- CUBIT, 2017. CUBIT 15.3 User Documentation, Sandia National Laboratories [Online; accessed 27-Jan-2017].
- Curnier, A., 1983. A static infinite element, *Int. J. Numer. Method. Eng.*, 19(10), 1479–1488.

- Dahlen, F.A. & Tromp, J., 1998. Theoretical Global Seismology, Princeton University Press.
- Deville, M.O., Fischer, P.F. & Mund, E.H., 2002. High-Order Methods for Incompressible Fluid Flow, Cambridge University Press.
- Douilly, R., Aochi, H., Calais, E. & Freed, A.M., 2015. Three dimensional dynamic rupture simulations across interacting faults: the mw7.0, 2010, haiti earthquake, J. geophys. Res.: Solid Earth, 120(2), 1108–1128.
- El-Esnawy, N.A., Akl, A.Y. & Bazaraa, A.S., 1995. A new parametric infinite domain element, *Finite Elem. Anal. Des.*, 19(1-2), 103–114.
- Faccioli, E., Maggio, F., Paolucci, R. & Quarteroni, A., 1997. 2D and 3D elastic wave propagation by a pseudo-spectral domain decomposition method, *J. Seismol.*, 1, 237–251.
- Frankel, A. & Vidale, J., 1992. A three-dimensional simulation of seismic waves in the Santa Clara Valley, California, from a Loma Prieta aftershock, *Bull. seism. Soc. Am.*, 82(5), 2045–2074.
- Freed, A.M., Bürgmann, R., Calais, E., Freymueller, J. & Hreinsdóttir, S., 2006. Implications of deformation following the 2002 Denali, Alaska, earthquake for postseismic relaxation processes and lithospheric rheology, J. geophys. Res.: Solid Earth, 111(B1).
- Gharti, H.N. & Tromp, J., 2017. A spectral-infinite-element solution of poisson's equation: an application to self gravity, preprint (arXiv:1706.00855).
- Gharti, H.N., Komatitsch, D., Oye, V., Martin, R. & Tromp, J., 2012a. Application of an elastoplastic spectral-element method to 3D slope stability analysis, *Int. J. Numer. Method. Eng.*, 91, 1–26.
- Gharti, H.N., Oye, V., Komatitsch, D. & Tromp, J., 2012b. Simulation of multistage excavation based on a 3D spectral-element method, *Comput. Struct.*, 100–101, 54–69.
- Gharti, H.N., Langer, L., Roth, M., Tromp, J., Vaaland, U. & Yan, Z., 2017.
 MeshAssist: an open-source and cross-platform meshing assistant tool, doi:10.5281/zenodo.883448.
- Gharti, H.N., Tromp, J. & Zampini, S., 2018. Spectral-infinite-element simulations of gravity anomalies, *J. geophys. Int.*, **215**(2), 1098–1117.
- Gropp, W., Lusk, E. & Skjellum, A., 1994. Using MPI, Portable Parallel Programming with the Message-Passing Interface, MIT Press.
- Hsu, Y.-J., Simons, M., Williams, C. & Casarotti, E., 2011. Threedimensional fem derived elastic green's functions for the coseismic deformation of the 2005 mw 8.7 nias-simeulue, sumatra earthquake, *Geochem. Geophys. Geosyst.*, 12(7), Q07013.

- Hu, Y., Wang, K., He, J., Klotz, J. & Khazaradze, G., 2004. Three-dimensional viscoelastic finite element model for postseismic deformation of the great 1960 chile earthquake, *J. geophys. Res.: Solid Earth*, 109(B12), 1–14.
- Kenner, S. & Segall, P., 1999. Time-dependence of the stress shadowing effect and its relation to the structure of the lower crust, *Geology*, 27(2), 119–122.
- Kenner, S.J. & Segall, P., 2000a. Postseismic deformation following the 1906 san francisco earthquake, *J. geophys. Res.: Solid Earth*, **105**(B6), 13195–13209
- Kenner, S.J. & Segall, P., 2000b. A mechanical model for intraplate earth-quakes: application to the New Madrid seismic zone, *Science*, 289(5488), 2329–2332
- Komatitsch, D. & Tromp, J., 1999. Introduction to the spectral element method for three-dimensional seismic wave propagation, *J. geophys. Int.*, 139, 806–822.
- Komatitsch, D. & Vilotte, J.P., 1998. The spectral element method: an efficient tool to simulate the seismic response of 2D and 3D geological structures, *Bull. seism. Soc. Am.*, 88(2), 368–392.
- Kumar, P., 1985. Static infinite element formulation, J. Struct. Eng., 111(11).
 Kyriakopoulos, C., Masterlark, T., Stramondo, S., Chini, M. & Bignami, C.,
 2013. Coseismic slip distribution for the mw 9 2011 Tohoku-oki earth-quake derived from 3-d fe modeling, J. geophys. Res.: Solid Earth, 118(7),
 3837–3847.
- Langer, L., Gharti, H.N. & Tromp, J., 2018. Impact of topography and threedimensional heterogeneity on coseismic deformation, *J. geophys. Int.*, submitted
- Marques, J.M.M.C. & Owen, D.R.J., 1984. Infinite elements in quasi-static materially nonlinear problems, *Comput. Struct.*, 18(4), 739–751.
- Marques, S.P.C. & Creus, G.J., 2012. Computational Viscoelasticity, Springer.
- Masterlark, T., 2003. Finite element model predictions of static deformation from dislocation sources in a subduction zone: sensitivities to homogeneous, isotropic, Poisson-solid, and half-space assumptions, *J. geophys. Res.: Solid Earth*, **108**(B11).
- Mavriplis, C., 1989. Laguerre polynomials for infinite-domain spectral elements, J. Comput. Phys., 80(2), 480–488.
- Medina, F. & Taylor, R.L., 1983. Finite element techniques for problems of unbounded domains, *Int. J. Numer. Method. Eng.*, 19(8), 1209–1226.
- Melosh, H.J. & Raefsky, A., 1981. A simple and efficient method for introducing faults into finite element computations, *Bull. seism. Soc. Am.*, 71(5), 1391–1400.
- Nur, A. & Mavko, G., 1974. Postseismic viscoelastic rebound, *Science*, 183(4121), 204–206.
- Okada, Y., 1985. Surface deformation due to shear and tensile faults in a half-space, *Bull. seism. Soc. Am.*, **75**(4), 1135–1154.
- Okada, Y., 1992. Internal deformation due to shear and tensile faults in a half-space, *Bull. seism. Soc. Am.*, **82**(2), 1018–1040.
- Parker, J., Lyzenga, G., Norton, C., Zuffada, C., Glasscoe, M., Lou, J. & Donnellan, A., 2008. Geophysical finite-element simulation tool (GeoFEST):

- algorithms and validation for quasistatic regional faulted crust problems, *Pure appl. Geophys.*, **165**(3), 497–521.
- Patera, A.T., 1984. A spectral element method for fluid dynamics: laminar flow in a channel expansion, *J. Comput. Phys.*, **54**, 468–488.
- Pellegrini, F. & Roman, J., 1996. SCOTCH: a software package for static mapping by dual recursive bipartitioning of process and architecture graphs, *Lecture Notes Comput. Sci.*, 1067, 493–498.
- Peter, D. et al., 2011. Forward and adjoint simulations of seismic wave propagation on fully unstructured hexahedral meshes, *J. geophys. Int.*, **186**(2), 721–739
- Piersanti, A., Spada, G., Sabadini, R. & Bonafede, M., 1995. Geobal postseismic deformation, *Geophys. J. Int.*, 120(3), 544–566.
- Pollitz, F.F., 1992. Postseismic relaxation theory on the spherical earth, Bull. seism. Soc. Am., 82(1), 422.
- Pollitz, F.F., 1996. Coseismic deformation from earthquake faulting on a layered spherical earth, *J. geophys. Int.*, **125**(1), 1–14.
- Pollitz, F.F., 2014. Post-earthquake relaxation using a spectral element method: 2.5-D case, J. geophys. Int., 198(1), 308–326.
- Reilinger, R.E. *et al.*, 2000. Coseismic and postseismic fault slip for the 17 August 1999, m = 7.5, Izmit, Turkey earthquake, *Science*, **289**(5484), 1510, 1524
- Savage, J.C., 1998. Displacement field for an edge dislocation in a layered half-space, J. geophys. Res.: Solid Earth, 103(B2), 2439–2446.
- Savage, J.C. & Prescott, W.H., 1978. Asthenosphere readjustment and the earthquake cycle, J. geophys. Res.: Solid Earth, 83(B7), 3369–3376.
- Seriani, G. & Oliveira, S.P., 2008. Dispersion analysis of spectral-element methods for elastic wave propagation, *Wave Motion*, 45, 729–744.
- Simo, J.C. & Hughes, T.J.R., 1998. Computational Inelasticity, Springer.
- Tanaka, Y., Klemann, V., Fleming, K. & Martinec, Z., 2009. Spectral finite element approach to postseismic deformation in a viscoelastic self-gravitating spherical earth, *J. geophys. Int.*, 176(3), 715–739.
- Tromp, J., Komatitsch, D. & Liu, Q., 2008. Spectral-element and adjoint methods in seismology, Commun. Comput. Phys., 3(1), 1–32.
- Tsynkov, S.V., 1998. Numerical solution of problems on unbounded domains: a review, Appl. Numer. Math., 27(4), 465–532, .
- Wang, K. & Fialko, Y., 2018. Observations and modeling of coseismic and postseismic deformation due to the 2015 mw 7.8 Gorkha (Nepal) earthquake, J. geophys. Res.: Solid Earth, 123(1), 761–779.
- Williams, C.A. & Richardson, R.M., 1991. A rheologically layered threedimensional model of the San Andreas fault in Central and Southern California, *J. geophys. Res.: Solid Earth*, 96(B10), 16597–16623.
- Zhao, S., Müller, R.D., Takahashi, Y. & Kaneda, Y., 2004. 3-D finite-element modelling of deformation and stress associated with faulting: effect of inhomogeneous crustal structures, J. geophys. Int., 157(2), 629–644.
- Zienkiewicz, O.C. & Taylor, R.L., 2005. The Finite Element Method for Solid and Structural Mechanics, Elsevier Butterworth-Heinemann.
- Zienkiewicz, O.C., Emson, C. & Bettess, P., 1983. A novel boundary infinite element, *Int. J. Numer. Method. Eng.*, **19**(3), 393–404.
- Zienkiewicz, O.C., Taylor, R.L. & Zhu, J.Z., 2005. The Finite Element Method: Its Basis and Fundamentals, 6th edn, Elsevier Butterworth-Heinemann.